Chapter 7

Theory and Application of Adaptive Moving Grid Methods

P. A. Zegeling

Mathematical Institute
Utrecht University
Budapestlaan 6, 3584 CD, Utrecht
The Netherlands
zegeling@math.uu.nl

Contents

7.1   Introduction

Traditional numerical techniques to solve time-dependent partial differential equations (PDEs) integrate on a uniform spatial grid that is kept fixed on the entire time interval. If the solutions have

regions of high spatial activity, a standard fixed-grid technique is computationally inefficient, since to afford an accurate numerical approximation, it should contain, in general, a very large number of grid points. The grid on which the PDE is discretized then needs to be locally refined. Moreover, if the regions of high spatial activity are moving in time, like for steep moving fronts in reaction-diffusion or hyperbolic equations, then techniques are needed that also adapt (move) the grid in time.

In the realm of adaptive techniques for time-dependent PDEs we can, roughly spoken, distinguish between two classes of methods.

The first class, denoted by the term h-refinement, consists of so-called static-regridding methods. For these methods, the grid is adapted only at discrete time levels. The main advantage of this type of techniques is their conceptual simplicity and robustness, in the sense that they permit the tracking of a varying number of wave fronts. A drawback, however, is that interpolation must be used to transfer numerical quantities from the old grid to new grids. Also, numerical dispersion, appearing, for instance, when hyperbolic PDEs are numerically approximated, is not fully annihilated with h-refinement. Another disadvantage of static-regridding is the fact that it does not produce 'smoothing' in the time direction, with the consequence that the time-stepping accuracy therefore will demand small time steps. An example of such a method can be found in [4] or in [33].

The second class of methods, denoted by the term r-refinement (re-distribute or re-locate), have the special feature to move the spatial grid continuously and automatically in the space-time domain while the discretization of the PDE and the moving-grid procedure are intrinsically coupled. Moving-grid techniques use a fixed number of grid points, without need of interpolation and let the grid points dynamically move with the underlying feature of the PDE (wave, pulse, front, ...). Examples of r-refinement based methods can be found in [2, 9, 10, 17–19, 24, 26, 29, 37] and later on in this manuscript. Since the number of grid points is held fixed throughout the course of computation, problems could arise if several steep fronts would act in different regions of the spatial domain. For example, the grid is following one wave front, while a second front arises somewhere else. No 'new' grid is created for the new wave front, but rather the 'old' one has to adjust itself abruptly to cope with the newly-developed front. Another difficulty is of a topological nature: usually referred to as 'grid-distortion' or 'mesh-tangling'. Especially for higher dimensions this may cause problems, since the accuracy of the numerical approximation of the derivatives depends highly on the grid. Therefore, moving-grid techniques often need additional regularization terms to prevent this from happening or to at least slow down the grid degeneration process. In this paper, we will address different solutions to this regularization problem. Let us first concentrate on a PDE example in one space dimension to show the effectiveness of adaptive moving grids. After that, we will develop gradually some theory starting with the stationary case, extending it to time-dependent models and give an extensive set of applications from different areas, such as reaction-diffusion systems, medical applications, brine transport and magneto-hydrodynamics.

Consider the partial differential equation (PDE):

$$\frac{\partial u}{\partial t} - x\frac{\partial u}{\partial x} = 0, \ \ x \in [-3, 3] \tag{7.1.1}$$

which has the exact solution (using the correct boundary and initial condition)

$$u(x, t) = e^{-(e^t x)^2}.$$

N	$\|e\|_\infty$: (unif.) $t = 5$	(adapt.) $t = 5$	(unif.) $t = 10$	(adapt.) $t = 10$
100	0.669504	0.050343	0.993392	0.144466
200	0.506568	0.018615	0.988101	0.040614
400	0.322038	0.008071	0.978686	0.017416
800	0.161977	0.003626	0.962241	0.008049
1600	0.060010	0.001640	0.934068	0.003819

Table 7.1: Uniform and adaptive grid results for PDE model (7.1.1) at two points of time for an increasing number of spatial grid points N; $\|e\|_\infty$ denotes the maximum error.
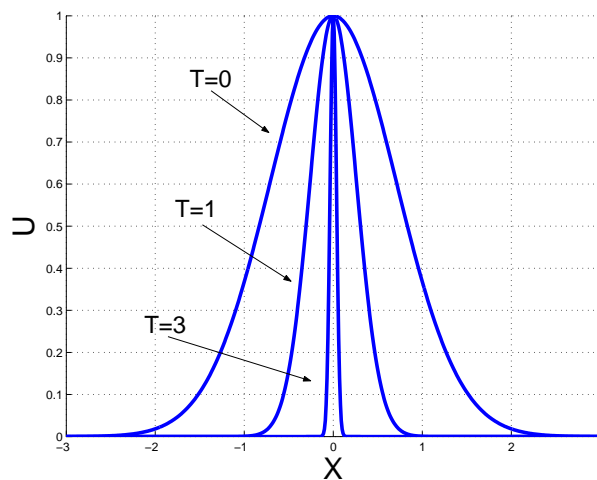
Figure 7.1: The exact solution of equation (7.1.1) for increasing time.

The solution (see also Figure 7.1) can be derived by examining the characteristics of the PDE:

$$\left\{ \begin{array}{l} \dot{x} = -x, \\ \dot{u} = 0. \end{array} \right.$$

This concept can be interpreted as follows: the maximum of the solution stays equal to the value 1 for all time t ($\dot{u} = 0$), but the steepness of the wave increases, because of the 'implosion' caused by the fact that the characteristic trajectories satisfy $\dot{x} = -x$. In Table 7.1 a comparison is made between the numerical solution on a uniform grid and an adaptive moving grid (details found in Section [41]) for two different points of time using an implicit Euler method for the time integration (within the code DASSL [28] with a time-tolerance of 10^{-8} and central finite differences for the spatial derivatives). It it obvious from the numerical results in Table 7.1 to conclude that adaptive moving grids are useful for models in which steep moving transitions play an important role. Figure 7.2 shows the adaptive grid as a function time and also the differences between a typical uniform and moving non-uniform experiment.
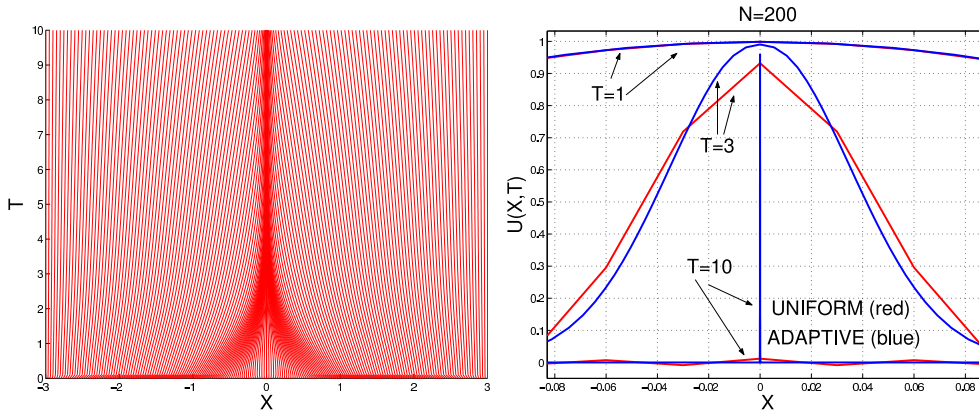
Figure 7.2: Adaptive moving grid solution of (7.1.1); left panel: time-dependent grid history, right panel: numerical solutions for 201 grid points (zoomed in around the 'singularity' $x = 0$).

7.2   Adaptive moving grids in one dimension

7.2.1   A simple boundary-value problem

Consider the following time-*in*dependent boundary-value model (BV-model):

$$\varepsilon u_{xx} - u_x = 0, \;\; u(0) = 0, \; u(1) = 1 \tag{7.2.1}$$

which has the exact solution: $u(x) = \frac{e^{\frac{x}{\varepsilon}} - 1}{e^{\frac{1}{\varepsilon}} - 1}$ (see Figure 7.3; left panel). The solution is monotonically increasing, with a boundary layer being formed near $x = 1$ of size $\mathcal{O}(\varepsilon)$ for values $0 < \varepsilon \ll 1$. We will apply three basic numerical approaches to approximate solutions of equation (7.2.1).
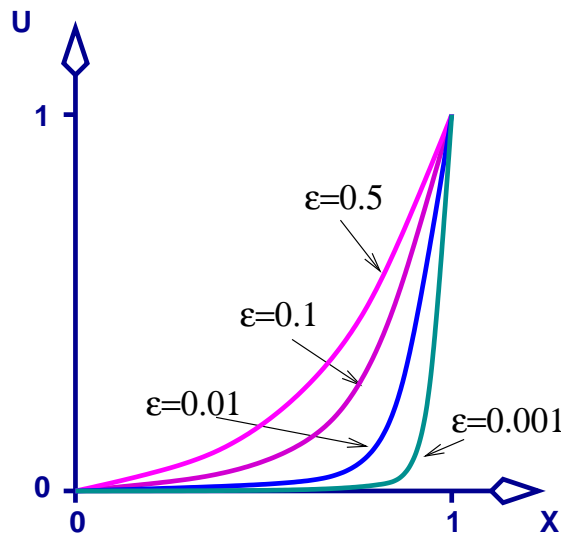
Figure 7.3: The exact solution of BV-model (7.2.1) for decreasing values of ε.

Numerical approximation (idea 1):

$$\varepsilon \frac{u_{i+1} - 2u_i + u_{i-1}}{\Delta x^2} - \frac{u_{i+1} - u_{i-1}}{2\Delta x} = 0, \; i = 1 : N - 1. \tag{7.2.2}$$

This approximation is obtained by applying central finite differences to the first and second derivatives in (7.2.1). The exact numerical solution (i.e. the exact solution of the discretized system (7.2.2)) reads:

$$u_i = \frac{(\frac{1+P_e}{1-P_e})^i - 1}{(\frac{1+P_e}{1-P_e})^N - 1},$$

with mesh-Peclet number $P_e := \frac{\Delta x}{2\varepsilon}$ and cell-size $\Delta x = \frac{1}{N}$. From this expression we can make the following statements:

$\star$ for $N < \frac{1}{2\varepsilon} \rightsquigarrow P_e > 1$: the numerical solution *oscillates* (see also Figure 7.4, left panel).

$\star$ for $N > \frac{1}{2\varepsilon} \rightsquigarrow 0 < P_e < 1$: *monotone* numerical values are obtained.

$\star$ for $0 < \varepsilon \ll 1$ we need $N \ggg 1$ to satisfy this monotonicity condition, which leads to a highly inefficient numerical process.

$\star$ The numerical error behaves like: $\mathcal{O}(\Delta x^2) = \mathcal{O}(\frac{1}{N^2})$.
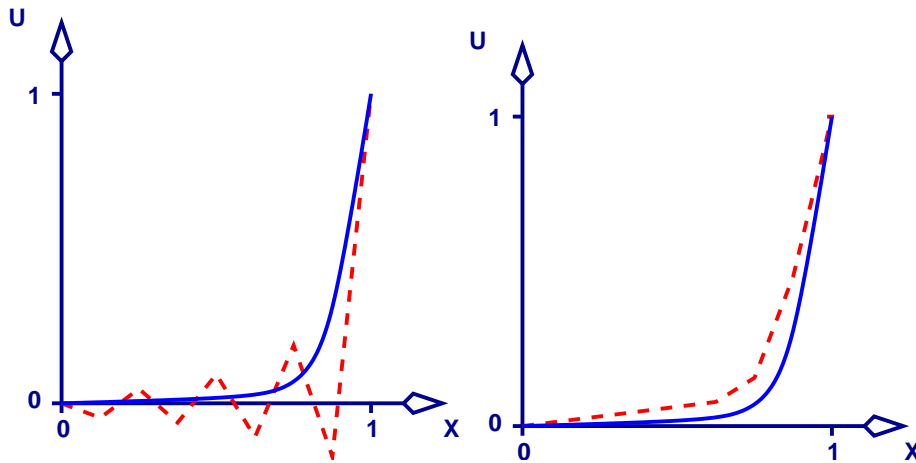
Figure 7.4: Numerical (−) vs. exact solutions of BV-model (7.2.1); method I (left panel) and method II (right panel).

Numerical approximation (idea 2):

$$\varepsilon \frac{u_{i+1} - 2u_i + u_{i-1}}{(\Delta x)^2} - \frac{u_i - u_{i-1}}{\Delta x} = 0, \; i = 1 : N - 1. \tag{7.2.3}$$

This approximation represents an upwind discretization of the first derivative in model (7.2.1). The exact solution of system (7.2.3) reads:

$$u_i = \frac{(1 + P_e)^i - 1}{(1 + P_e)^N - 1}.$$

Similar to the previous approximation (7.2.2), we can work out a few results for this approximation:

$\star$ $1 + P_e > 1 \Longrightarrow u_{i+1} > u_i \ \forall i$: we always get a *monotone* numerical solution.

$\star$ Unfortunately, the error behaves now as: $\mathcal{O}(\Delta x) = \mathcal{O}(\frac{1}{N})$, which is worse than for the previous case.

$\star$ Moreover, additional numerical damping ("diffusion") is introduced in the numerical system:

$$\frac{u_i - u_{i-1}}{\Delta x} = \frac{u_{i+1} - u_{i-1}}{2\Delta x} - \frac{\Delta x}{2} \frac{u_{i+1} - 2u_i + u_{i-1}}{\Delta x^2}.$$

(see also Figure 7.4, right panel)

Numerical approximation (idea 3):

Define $v(\xi) := u(x(\xi))$ and a transformation $x \longmapsto \xi \in [0, 1]$. Then BV-problem (7.2.1) is transformed to

$$\frac{\varepsilon}{x_\xi} \left[\frac{v_{\xi\xi} x_\xi - v_\xi x_{\xi\xi}}{x_\xi^2} \right] - \frac{v_\xi}{x_\xi} = 0.$$

Suppose that we map the steep solution $u(x)$ in the x-coordinates to the mild (linear) function $v(\xi) = \xi$ in the ξ-coordinates and assume $x_\xi > 0$ ('the transformation is regular'), then

$$\varepsilon x_{\xi\xi} + x_\xi^2 = 0, \ \ x(0) = 0, \ x(1) = 1$$

which has the exact solution $x(\xi) = \varepsilon \ln(\xi(e^{\frac{1}{\varepsilon}} - 1) + 1)$. It is easy to derive that the following identity holds for this particular mapping

$$x_\xi u_x = 1, \tag{7.2.4}$$

since $u_x = \frac{v_\xi}{x_\xi}$ and $v_\xi = 1$. Note that x_ξ is related to the inverse of the grid point concentration of the non-uniform grid. From these expressions can also be derived that: if u_x is *large* then x_ξ is *small* and vice versa, i.e., grid points are concentrated in the boundary layer of model (7.2.1) (see Figures 7.5 and 7.6). Equation (7.2.4) is identical to

$$x_\xi \, \omega = 1 \tag{7.2.5}$$

where $\omega := u_x > 0$ is a so-called 'monitor' function. The question is: can we use this principle, or a similar one, for more general situations as well?

7.2.2   The equidistribution principle

We have seen that principle (7.2.5) can be useful to let the grid points be concentrated in regions with high first order spatial derivatives. In general, we can define such a principle in terms of a more general monitor or weight function ω to obtain the so-called equidistribution principle, originally worked out by [7] in the context of spline approximations. The idea behind this method is that we want to "equally distribute" the positive definite monitor function ω on a non-uniform grid. Ideally, ω represents some kind of measure of the error of the underlying numerical scheme. To get some better idea of this method we first define a non-uniform grid

$$x_L = x_0 < x_1 < x_2 < ... < x_{N-1} < x_N = x_R$$
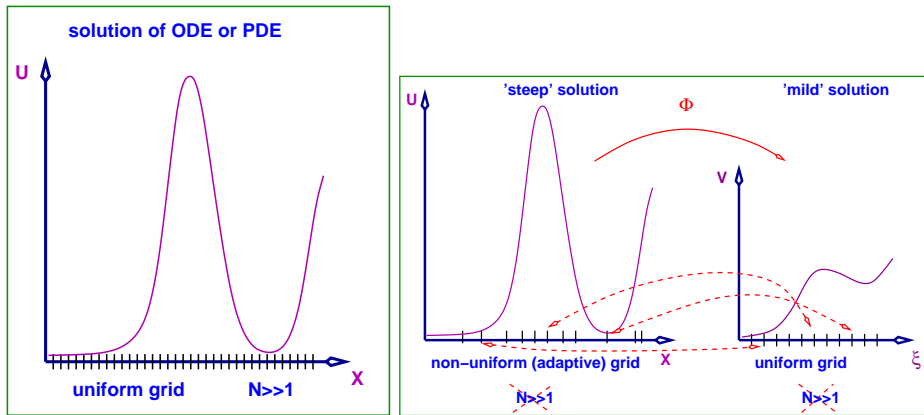
Figure 7.5: The non-uniform adaptive grid seen as a coordinate transformation between physical x and computational coordinates ξ.
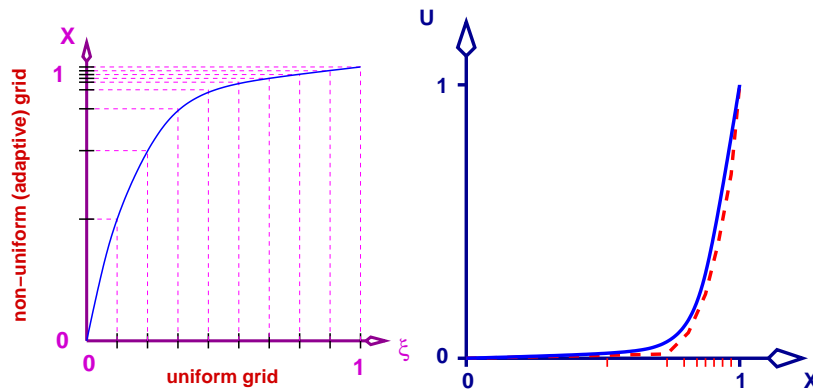
Figure 7.6: Numerical approximation of BV-model (7.2.1) using method III (left panel: the non-uniform grid in terms of the coordinate transformation; right panel: exact vs. numerical solution).

and try to find the actual grid point distribution such that the contribution to the 'error' from each subinterval (x_{i-1}, x_i) is the same. The basic principle then reads (the connection with (7.2.5) will soon become clear):

$$\Delta x_i \, \omega_i = c, \ \ i = 0, ..., N - 1. \tag{7.2.6}$$

with $x_0 = x_L$, $x_N = x_R$, $\Delta x_i := x_{i+1} - x_i$, which is a discrete version of (after having applied the midpoint rule to the integral):

$$\int_{x_i}^{x_{i+1}} \omega \, dx = c, \ \ i = 0, ..., N - 1.$$

The constant c is determined from:

$$\int_{x_L}^{x_R} \omega \, dx = \int_{x_0}^{x_1} \omega \, dx + \int_{x_1}^{x_2} \omega \, dx + ... + \int_{x_{N-1}}^{x_N} \omega \, dx = c + c + ... + c \ \ (N \text{ times}),$$

giving $c = \frac{1}{N} \int_{x_L}^{x_R} \omega dx$. We then obtain:

$$\int_{x_i}^{x_{i+1}} \omega dx = \frac{1}{N} \int_{x_L}^{x_R} \omega dx, \;\; i = 0, ..., N-1,$$

from which we read that the monitor function ω is indeed equally distributed over all subintervals, thereby clarifying the name of the principle. From (7.2.6) the main idea behind this principle becomes clear as well: grid cells Δx_i are small where ω_i is large, and vice versa, *since* their product is constant. In fact this is the discrete version of the continuous formulation (7.2.5). Equation (7.2.6) can also be interpreted as an approximation to the problem

$$x_\xi \omega = c, \;\; 0 < \xi < 1$$

or, taking the ξ-derivative, to the boundary-value problem

$$(\omega x_\xi)_\xi = 0, \quad x(0) = x_L, \;\; x(1) = x_R. \tag{7.2.7}$$

Note that since $\frac{dx}{d\xi} = \frac{1}{\frac{d\xi}{dx}}$, we find

$$\frac{d\xi}{dx} = c\,\omega, \;\; x_L < x < x_R, \; \xi(x_L) = 0, \; \xi(x_R) = 1.$$

From this follows the relation

$$1 = 1 - 0 = \xi(x_R) - \xi(x_L) = \int_{x_L}^{x_R} \frac{d\xi}{dx}\,dx = c \int_{x_L}^{x_R} \omega dx,$$

so that the constant c can be written as $c = \frac{1}{\int_{x_L}^{x_R} \omega dx}$ and therefore $\frac{d\xi}{dx} = \frac{\omega}{\int_{x_L}^{x_R} \omega dx}$. If we now integrate the expresssion

$$\frac{d\xi}{dx} = \frac{\omega}{\int_{x_L}^{x_R} \omega d\bar{x}}$$

we arrive at an explicit formula for the *inverse* coordinate transformation:

$$\xi(x) = \int_{x_L}^{x} \frac{\omega}{\int_{x_L}^{x_R} \omega d\bar{x}} d\bar{x} = \frac{\int_{x_L}^{x} \omega d\bar{x}}{\int_{x_L}^{x_R} \omega d\bar{x}}.$$

We already mentioned that $\xi_x = \frac{1}{x_\xi}$ represents the 'grid point density' of the transformation. What about the regularity of the transformation? Can the grid points cross each other and destroy the 'topology', i.e. the natural ordering, of the grid point distribution? The answer to this question is, fortunately, negative and can be easily checked by working out the following identity, which is a direct result of the previous calculations:

$$\frac{dx}{d\xi}\omega = c = \frac{x_R - x_L}{\int_0^1 \omega d\bar{\xi}}.$$

For $\omega > 0$ we have $c > 0$, and thus $\frac{dx}{d\xi} > 0$ (by definition: $x_R - x_L > 0$). The Jacobian of the transformation is given by $\frac{dx}{d\xi} > 0$ from which we may conclude that the transformation is non-singular. In terms of the grid points this reads $\Delta x_i \omega_i = c > 0 \Rightarrow \Delta x_i > 0$: the grid points do not cross!

It is interesting to note that the equidistribution principle, as just described, can be derived from a variational formulation. To see this, we consider the 'grid-energy'

$$\mathcal{E} = \int_0^1 \omega x_\xi^2 d\xi$$

and minimizing this energy functional, in a straightforward manner, via the Euler-Lagrange equation:

$$\frac{d}{d\xi}\left(\frac{\partial \mathcal{F}}{\partial x_\xi}\right) - \frac{\partial \mathcal{F}}{\partial x} = 0 \ \text{ with } \ \mathcal{F} = \mathcal{F}(x, x_\xi) = \omega(\xi)x_\xi^2 \ \text{ gives:}$$

$$\frac{d}{d\xi}(2\omega x_\xi) - 0 = 0 \Leftrightarrow \boxed{\frac{d}{d\xi}\left[\omega \frac{dx}{d\xi}\right] = 0}$$

which is equal to the differential formulation (7.2.7)! The 'grid-energy' can be taken to represent the energy of a system of springs with spring constants ω spanning each interval and connecting points of mass (grid points). The non-uniform grid point distribution resulting from the equidistribution principle thus represents the equilibrium state of the spring system, i.e., the state of minimum energy (see also Figure 7.7).
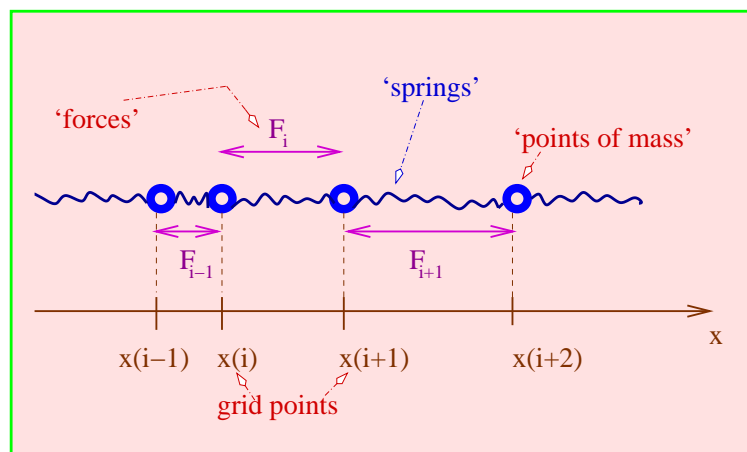
Figure 7.7: The non-uniform adaptive grid seen as a system of 'springs' connecting 'points of mass'.

We still can not apply principle (7.2.7), since we do not know yet how to choose the monitor function ω. A first choice, see (7.2.4), may be $\omega = u_x$. This yields $x_\xi \omega = x_\xi u_x = x_\xi \frac{v_\xi}{x_\xi} = v_\xi = c$. In words: the grid points x_i adjust in such a way that the same change in the solution u occurs over each grid interval (x_{i-1}, x_i). The main disadvantage is the fact that, if $u_x \downarrow 0$, then $\Delta x_i \to \infty$ (the transformation becomes singular), see Figure 7.8 (left panel).

An alternative choice for ω is to take $\sqrt{1 + u_x^2}$ (Figure 7.8; right panel). In this case an increment of *arclength ds* on the solution curve $u(x)$ is given by $ds^2 = dx^2 + du^2 = (1 + u_x^2)dx^2$ from which we obtain $\omega = s_x$ and thus $x_\xi s_x = x_\xi \frac{s_\xi}{x_\xi} = s_\xi = c$. The grid point distribution is now such that
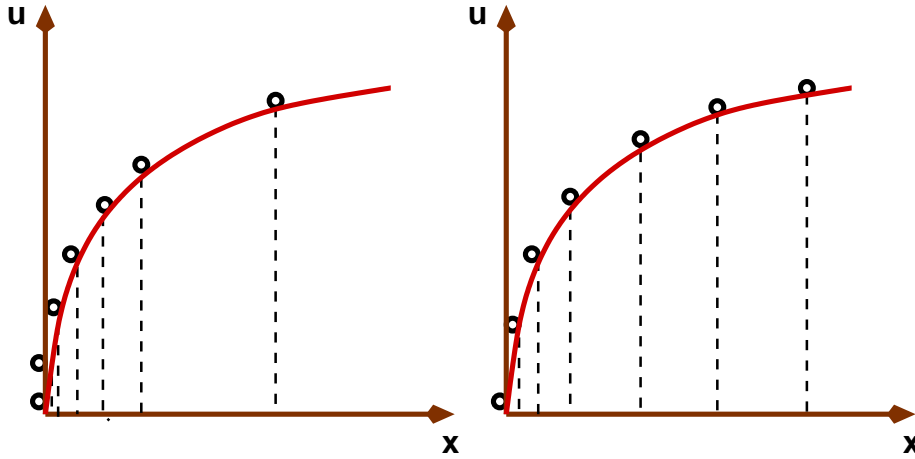
Figure 7.8: Grid point distribution using $\omega = u_x$ (left) and arclength monitor (right).

the same increment in arclength in the solution occurs over each subinterval in the non-uniform grid distribution. Note that here $u_x \downarrow 0 \Rightarrow \Delta x_i \to \frac{1}{N}$, i.e. for low values of the gradient u_x, the grid points are distributed uniformly (in the limit). Many other possible choices for ω have been used in the literature. In [38] a few other choices and references are given. In practical applications the scaling of the solution u and the dimension of the spatial domain x may influence the grid distribution induced by $\omega = \sqrt{1 + u_x^2}$. Therefore, often a extra constant α is added to the monitor function: $\omega = \sqrt{\alpha + u_x^2}$ or $\omega = \sqrt{1 + \alpha u_x^2}$ to take into account these scaling effects. This, of course, may result in a user-unfriendly method, since the α depends on the particular PDE model. A more sophisticated monitor function taken from [15] will be given in Section 7.2.4 in which a 'solution-adaptive' parameter in ω is used to cope with this scaling problem . Additional information can also be found in the description of the higher-dimensional case later on. Furthermore, the extension of the equidistribution principe to time-dependent differential equations is straightforward: the grid distribution Δx_i will depend on time t:, i.e. $\Delta x_i(t)$, just as the constant c in, for instance, (7.2.6).

7.2.3   Smoothing of the grid in space and time

Besides the issue how to choose the monitor function in (7.2.7), we might conclude that the just-mentioned equidistribution principle in the current form may be used efficiently for general PDE models. But the question to be answered is:

Does 'pure' equidistribution suffice?

In order to get an answer to this question it may be illustrative to consider two diierent PDE models. The first one is the well-known viscous Burgers' equation which reads

$$\frac{\partial u}{\partial t} + u\frac{\partial u}{\partial x} = 5 \ 10^{-3}\frac{\partial^2 u}{\partial x^2}, \ x \in [0, 1]. \tag{7.2.8}$$

As initial condition and boundary conditions we take $u(x, 0) = \sin(\pi x)$, $u(0, t) = u(1, t) = 0$. The solution starts smoothly, but will develop a sharp transition layer near $x = 1$. What happens with the equidistribution grid with $\omega = \sqrt{1 + u_x^2}$ we can see in Figure 7.9. On the left the solution and the grid are shown. Both the grid trajectories and the solution itself appear to be irregular ('unsmooth'). In the same figure, now in the right panel, the same method is being used, but with additional smoothing. This will be explained later on.
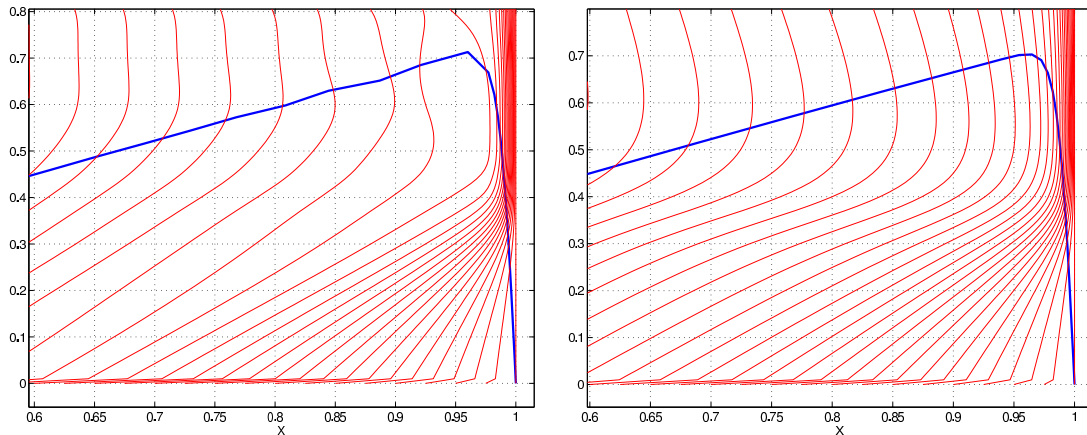
Figure 7.9: Adaptive moving grid solutions of (7.2.8) on a non-smooth grid (left) and on a smoother grid (right) with the same number of grid points.

A second example is given by the hyperbolic PDE

$$\frac{\partial u}{\partial t} + 4\cos(4\pi t)\frac{\partial u}{\partial x} = 0. \tag{7.2.9}$$

An exact solution of this hyperbolic PDE is

$$u(x, t) = \sin^{1000}\left(\pi\left(x - \frac{1}{\pi}\sin(4\pi t)\right)\right)$$

which describes an *extremely sharp* pulse that *moves periodically* in the time direction, from left to right and backwards again through the spatial domain. Similar to the Burgers' model we show the solution (on a uniform grid, an unsmooth equidistributed grid and a smoothed equidistribution grid) in Figures 7.10 and 7.11, respectively. Obviously we need extra smoothing on top of the equidistribution principle (7.2.5). First we need to identify and quantify these unsmooth effects. We will see that this can be done in terms of

- *local truncation errors* on non-uniform grids and

- *unsmoothness and instability of a time-dependent grid* based on *pure* equidistribution.

For this purpose, we define the 'grid size ratio' ('local stretching factor'):

$$r := \frac{x_i - x_{i-1}}{x_{i+1} - x_i} := \frac{\Delta x_{i-1}}{\Delta x_i} := \frac{q}{p}.$$
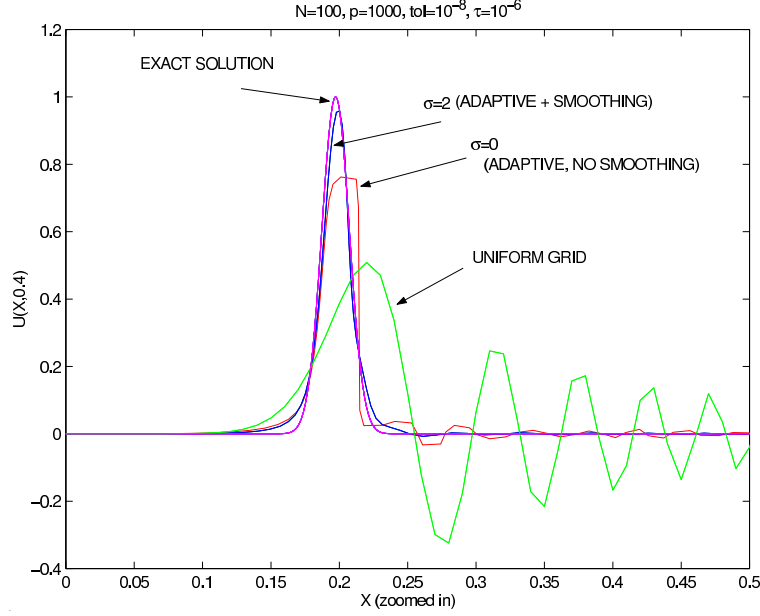
Figure 7.10: Comparison of uniform grid and adaptive moving grid solutions (smooth vs unsmooth) for model (7.2.9).

Using a Taylor expansion, it follows that the truncation error T for the central finite difference approximation (on a non-uniform grid) $u_{x,i} \approx \frac{u_{i+1}-u_{i-1}}{p+q}$ is given by

$$
\begin{aligned}
&= -\frac{p^2 - q^2}{2(p+q)}u_{xx,i} - \frac{p^3 + q^3}{6(p+q)}u_{xxx,i} + ... \\
&= -\frac{1}{2}u_{xx,i}(1-r)\Delta x_i - \frac{1}{2}u_{xxx,i}(1 - r + r^2)\Delta x_i^2 + ... \\
&= \frac{\Delta\xi^2}{6}(3x_{\xi\xi,i}u_{xx,i} + x_\xi^2 u_{xxx,i}) + \mathcal{O}(\Delta\xi^4) \\
&= \Delta x_i^2 \left(\frac{1}{2}\frac{x_{\xi\xi,i}}{x_{\xi,i}}u_{xx,i} + \frac{1}{6}u_{xxx,i}\right) + \mathcal{H.O.T.}
\end{aligned}
$$

We immediately see that for $r = 1$ (a uniform grid) the numerical approximation is of *second-order*:

$$
T = -\frac{\Delta\xi^2}{6}u_{xxx,i} + \mathcal{O}(\Delta\xi^4).
$$

However, for the non-uniform grid case, $r \neq 1$, and the approximation is of *second order*, only if $r = 1 + \mathcal{O}(\Delta x_i)$. Since

$$
r = \frac{x_{\xi,i}\Delta\xi - \frac{1}{2}\Delta\xi^2 x_{\xi\xi,i}}{x_{\xi,i}\Delta\xi + \frac{1}{2}\Delta\xi^2 x_{\xi\xi,i}} + \mathcal{H.O.T.} = 1 - \Delta x_i \frac{x_{\xi\xi,i}}{x_{\xi,i}^2} + \mathcal{H.O.T.}
$$

we can conclude that $\frac{x_{\xi\xi,i}}{x_{\xi,i}^2} = \mathcal{O}(1) \Leftrightarrow r = 1 + \mathcal{O}(\Delta x_i)$. If the ratio $\frac{x_{\xi\xi,i}}{x_{\xi,i}^2}$ is too big, then $r \neq \mathcal{O}(1)$ and this influences the order of the truncation error. Grids with $r = 1 + \mathcal{O}(\Delta x_i)$ are called 'quasi-uniform'.
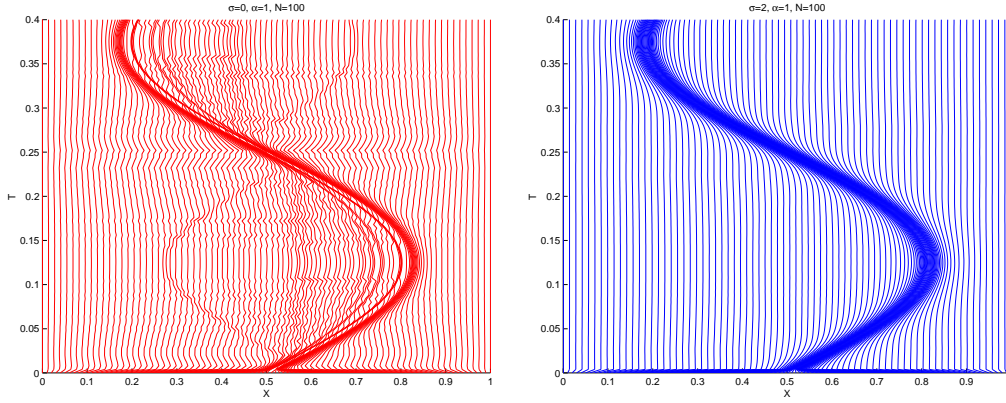
Figure 7.11: Unsmooth vs smoothed adaptive moving grids for PDE model (7.2.9).

Such grids (in terms of the transformation: $\frac{x_{\xi\xi,i}}{x_{\xi,i}^2} = \mathcal{O}(1)$) are 'smooth' enough and will not change greatly between adjacent intervals. How to adjust the equidistribution principle to guarantee this, we will see in Section 7.2.3.

A second potential problem with the basic equidistribution principle can be explained as follows: if we differentiate the equidistribution relation

$$\int_{x_L}^{x_i(t)} \omega dx = \frac{i}{N} \int_{x_L}^{x_R} \omega dx := \frac{i}{N} \omega(t), \ \ i = 1, ..., N$$

with respect to time t we obtain

$$\omega(x_i, t)\dot{x}_i + \int_{x_L}^{x_i} \frac{\partial \omega}{\partial t}(x, t)dx = \frac{i}{N}\dot{\omega}(t), \ \ i = 1, ..., N.$$

Introducing small perturbations δx_i on the grid points x_i and using Taylor expansions for $\omega(x_i + \delta x_i, t)$ and $\int_{x_L}^{x_i + \delta x_i} \frac{\partial \omega}{\partial t}dx$ we get

$$\omega(x_i, t)\dot{x}_i + \frac{\partial \omega}{\partial x}\delta x_i \dot{x}_i + \omega(x_i, t)\delta \dot{x}_i + \int_{x_L}^{x_i} \frac{\partial \omega}{\partial t}dx + \frac{\partial \omega}{\partial t}\delta x_i + \mathcal{H.O.T.} = \frac{i}{N}\dot{\omega}(t).$$

After linearization follows

$$\omega(x_i, t)\delta \dot{x}_i + \frac{\partial \omega}{\partial x}\delta x_i \dot{x}_i + \frac{\partial \omega}{\partial t}\delta x_i = 0.$$

This is equivalent with $\frac{d}{dt}[\omega(x_i(t), t)\delta x_i] = 0$ and integrating once gives

$$\omega(x_i(t), t)\delta x_i(t) = \text{CONSTANT} = \omega(x_i(0), 0)\delta x_i(0)$$

and therefore $\delta x_i(t) = \frac{\omega(x_i(0), 0)}{\omega(x_i(t), t)}\delta x_i(0)$. From this expression we see that, if $\frac{\omega(x_i(0), 0)}{\omega(x_i(t), t)}$ becomes > 1, the adaptive grid in equidistribution may become *unstable*. This may be prevented by adding a small 'delay'-term to the equidistribution principle. More details on this kind of instability can be found in [14]. In the next section an alternative to the basic equidistribution formula will be derived.

How to deal with unsmoothness of the grid?

From the previous section we have learned that an important inequality for the non-uniform grid is given by

$$\frac{1}{K} \le r \le K, \quad K = \mathcal{O}(1).$$

Rewrite the time-dependent equidistribution principle $\Delta x_i \omega_i = c(t)$ in terms of 'point concentrations' $n_i := \frac{1}{\Delta x_i}$:

$$n_i = \bar{c}(t)\omega_i, \quad \forall i. \tag{7.2.10}$$

Next define

$$\breve{\omega}_i = \sum_{j=0}^{N} \omega_j \left(\frac{\sigma}{\sigma+1}\right)^{|i-j|}, \quad \sigma > 0, \;\; \omega > 0$$

and *replace* the (7.2.10) by

$$n_i = \bar{c}(t)\breve{\omega}_i, \quad \forall i. \tag{7.2.11}$$

This is in fact a spatially smoothed equidistribution principle. The following Lemma then holds (for the proofs of this and succeeding series of Lemma's we refer to [34]):

Lemma 7.2.1. *From $n_i = \bar{c}(t)\breve{\omega}_i$, $\forall i$, it follows* $\Rightarrow \frac{\sigma}{\sigma+1} \le \frac{n_i}{n_{i-1}} \le \frac{\sigma+1}{\sigma}$, $\forall i$.

An interesting observation is the fact that the magnitude of ω does not play a role at all in Lemma 7.2.1. Note that, if $\sigma = \mathcal{O}(1)$ then $r = \frac{n_i}{n_{i-1}} = \mathcal{O}(1)$ where the local stretching factor is written in terms of the point density instead of the cell-size. Define further $\tilde{n}_i := n_i - \sigma(\sigma+1)(n_{i+1} - 2n_i + n_{i-1}) = \tilde{c}(t)\omega_i$, $\forall i$ with 'Neumann' boundary conditions $n_0 = n_1$, $n_{N-1} = n_N$. Then the solution of this system of equations is given by

$$n_i = \tilde{c}\, C_+ \left(\frac{\sigma+1}{\sigma}\right)^i + \tilde{c}\, C_- \left(\frac{\sigma}{\sigma+1}\right)^i + \tilde{c} \sum_{j=1}^{N-1} \left(\frac{\sigma}{\sigma+1}\right)^{|i-j|}$$

for some constants C_+ and C_- that depend on the boundary values.

Lemma 7.2.2. *This solution n_i has also the property*

$$\frac{\sigma}{\sigma+1} \le \frac{n_i}{n_{i-1}} \le \frac{\sigma+1}{\sigma}, \; \forall i.$$

Instead of $n_i = \bar{c}(t)\breve{\omega}_i$ which can be shown to be equivalent with $\tilde{n}_i = \tilde{c}(t)\omega_i$ we set (a smoothed equidistribution principle both in space *and* time direction):

$$\tilde{n}_i(t) + \tau_s \frac{d}{dt}\tilde{n}_i(t) = \tilde{c}(t)\omega_i, \; \forall i \tag{7.2.12}$$

with boundary conditions $n_0 = n_1$, $n_{N-1} = n_N$, $\forall t$. Note that the solution of this *ODE*-system can be obtained in terms of the integral equation:

$$\tilde{n}_i(t) = \exp(-t/\tau_s)[\tilde{n}_i(0) + \int_0^t \tau_s^{-1} \exp(s/\tau_s)c(s)\omega_i(s)ds], \; t \ge 0, \; \forall i.$$

If we apply, for example, implicit Euler to (7.2.12 we can make the following observations with respect to the parameter τ_s:

- for $\tau_s \to 0$: $\tilde{n}_i^{(n+1)} \approx c^{(n+1)} \omega_i^{(n+1)} \ \forall i$ in case of no smoothing in the time direction

- if $\tau_s \gg \Delta t$: $\tilde{n}_i^{(n+1)} \approx \tilde{n}_i^{(n)} \ \forall i$ too much temporal smoothing $\Rightarrow$ no grid adaptation

- if $\tau_s = \mathcal{O}(\Delta t)$: $\tilde{n}_i^{(n+1)} \approx \frac{1}{2}\tilde{n}_i^{(n)} + \frac{1}{2}c^{(n+1)}\omega_i^{(n+1)} \ \forall i$ (use old values of grid as well for adaptation).

It is easily seen that:

Lemma 7.2.3. *For $\sigma = \tau_s = 0$, i.e., no smoothing at all: $n_i = \bar{c}(t)\omega_i$) and $\omega > 0 \Rightarrow n_i > 0, \ \forall i$.*

For the case $\tau_s = 0, \ \sigma \neq 0$, we have observed that $\tilde{n}_i = \tilde{c}\omega_i \Leftrightarrow n_i = \bar{c}\breve{\omega}_i \ \forall i \ (\breve{\omega}_i > 0)$. From Lemma 7.2.3 it follows directly that $n_i > 0, \ \forall i$ (simply replace ω_i by $\breve{\omega}_i$).

Lemma 7.2.4. *If n_i is the solution given by*

$$n_i = \tilde{c}\, C_+ \left(\frac{\sigma+1}{\sigma}\right)^i + \tilde{c}\, C_- \left(\frac{\sigma}{\sigma+1}\right)^i + \tilde{c} \sum_{j=1}^{N-1} \left(\frac{\sigma}{\sigma+1}\right)^{|i-j|}$$

then, because $n_i > 0 \Rightarrow \tilde{n}_i > 0 \ \forall i$.

For the case $\tau_s \neq 0, \ \sigma = 0$: $n_i + \tau_s \frac{d}{dt}n_i = \hat{c}(t)\omega_i$, we have

Lemma 7.2.5. $n_i(0) > 0, \ \forall i \Rightarrow n_i(t) > 0 \ \forall i \ \forall t \geq 0.$

Combining all the previous results gives for the most general case (cf. (7.2.12):

Lemma 7.2.6. *The solution n_i (in terms of $\tilde{n}_i$) is a linear combination of $\tilde{n}_i$-values with only positive coefficients (i.e. $\tilde{n}_i > 0 \Rightarrow n_i > 0$).*

And finally:

Theorem 7.1. *I) $\Delta x_i(0) > 0 \ \forall i \Rightarrow \Delta x_i(t) > 0 \ \forall i, \ \forall t \geq 0$ and II) $\frac{\sigma}{\sigma+1} \leq \frac{\Delta x_{i+1}(t)}{\Delta x_i(t)} \leq \frac{\sigma+1}{\sigma}, \ \forall i, \ \forall t \geq 0.$*

From these results follows that the smoothed equidistribution principle (7.2.12) deals with, and solves, both identified potential problems as discussed in Section 7.2.3. As already mentioned, for more information on these theoretical results the reader is referred to [34]. We are now ready to apply the enhanced and improved method to a series of PDE models from different application areas.

Application to time-dependent PDEs

Consider the time-dependent diffusion-convection-reaction PDE:

$$\frac{\partial u}{\partial t} = \varepsilon \frac{\partial^2 u}{\partial x^2} - \beta \frac{\partial u}{\partial x} + s(u, x, t). \tag{7.2.13}$$

Application of the coordinate transformation

$$x = x(\xi, \theta), \qquad t = t(\xi, \theta) = \theta, \qquad \mathcal{J} := x_\xi.$$

to (7.2.13) yields $U_\theta - \frac{1}{\mathcal{J}} x_\theta U_\xi = \frac{\varepsilon}{\mathcal{J}} [\frac{1}{\mathcal{J}} U_\xi]_\xi - \frac{\beta}{\mathcal{J}} U_\xi + s(x, U, \theta)$. Semi-discretization in the spatial direction first (with a uniform distribution in the computational coordinate ξ) gives:

$$\dot{U}_i - \frac{U_{i+1} - U_{i-1}}{x_{i+1} - x_{i-1}} (\dot{x}_i - \beta) = \varepsilon \frac{\frac{U_{i+1} - U_i}{x_{i+1} - x_i} - \frac{U_i - U_{i-1}}{x_i - x_{i-1}}}{\frac{1}{2}(x_{i+1} - x_{i-1})} + s_i. \tag{7.2.14}$$

In addition to the discrete formulation (7.2.12) it is possible to write the adaptive non-uniform grid in terms of this transformation. Let therefore $x(\xi, \theta)$ be the solution of the time-dependent grid PDE:

$$[(\mathcal{S}(x_\xi) + \tau_s x_{\xi\theta})\omega]_\xi = 0, \tag{7.2.15}$$

where $\tau_s > 0$ is the temporal smoothing parameter as used in Section 7.2.3), $\omega = \sqrt{1 + \alpha(U_x)^2}$ the monitor function and α the so-called 'adaptivity parameter'. The spatial smoothing operator $\mathcal{S}$ in (7.2.15) is defined by:

$$\mathcal{S} = \mathcal{I} - \sigma(\sigma + 1)(\Delta\xi)^2 \frac{\partial^2}{\partial \xi^2},$$

with σ the spatial smoothing parameter from Section 7.2.3. Similar to the results for the discrete case, some properties of the grid can be derived.

- $\mathcal{J} = x_\xi > 0 \quad \forall\, \theta \in [0, T]$ which reads in discretized form (note: $\Delta\xi$ is constant) $\Delta x_i(\theta) > 0 \ \forall\, \theta \in [0, T]$ (no 'node-crossing' possible)
- $\left|\frac{x_{\xi\xi}}{x_\xi}\right| \leq \frac{1}{\sqrt{\sigma(\sigma+1)}\Delta\xi}$ with discretized version:

$$\frac{\sigma}{\sigma + 1} \leq \frac{\Delta x_{i+1}(\theta)}{\Delta x_i(\theta)} \leq \frac{\sigma + 1}{\sigma} \quad \forall\, \theta \in [0, T].$$

  ('local quasi-uniformity')

- $\tau_s = \sigma = 0 \Rightarrow x_\xi \omega = \text{constant} \ \forall\, \theta \in [0, T]$

$$\Leftrightarrow \ \xi(x, t) = \frac{\int_{x_L}^{x} \omega \, d\bar{x}}{\int_{x_L}^{x_R} \omega \, d\bar{x}}.$$

  (in discretized form: $\Delta x_i \cdot \omega_i = \text{constant} \ \forall\, \theta \in [0, T]$ (equidistribution of the arclength monitor)

For the three parameters τ_s, σ and α we can give a rule of thumb how to choose them in a particular application:

$$0 < \tau_s \leq 10^{-3} \times \text{timescale in PDE model},$$

$$\sigma = \mathcal{O}(1) \quad (\sigma = 2 \text{ suffices in general}).$$

Note, however, that the third parameter depends on the different scales in the PDE solution, which may not be known on forehand:

$$\alpha = \mathcal{O}(1) \quad \text{depends on } x\text{- and } U\text{-scale}.$$

Semi-discretization of the adaptive grid PDE (7.2.15) yields:

$$\left[\tilde{\Delta}x_{i+1} + \tau_s \frac{\mathrm{d}\Delta x_{i+1}}{\mathrm{d}\theta}\right]\omega_{i+1} - \left[\tilde{\Delta}x_i + \tau_s \frac{\mathrm{d}\Delta x_i}{\mathrm{d}\theta}\right]\omega_i = 0,$$

where $\tilde{\Delta}x_i = \Delta x_i - \sigma(\sigma+1)(\Delta x_{i+1} - 2\Delta x_i + \Delta x_{i-1})$. Note that we have used here the alternative formulation in terms of Δx_i rather than the one with n_i. The semi-discretized system can be written as an adaptive-grid ODE system:

$$\tau_s\,\mathbf{B}(\vec{X},\vec{U},\sigma,\alpha)\dot{\vec{X}} = \vec{\mathcal{H}}(\vec{X},\vec{U},\sigma,\alpha).$$

When coupled on the semi-discretized PDE system (7.2.14), we obtain a large, stiff, banded, non-linear ODE system, which can solved in the time-direction with a stiff ODE solver such as DASSL [6, 28]. The full 1D code, which can solve a general class of PDE models accompanied with different kinds of boundary conditions is freely available and can be downloaded from the webpage *http://www.math.uu.nl/people/zegeling/publist.html*.

7.2.4 Applications

In this section a set of applications is treated to show the usefulness and effectiveness of the adaptive moving grid method as described in Section 7.2.3.

The Gray-Scott reaction-diffusion system

A reaction-diffusion model in which several interesting phenomena from pattern formation can occur, is defined by the Gray-Scott PDE system [16]:

$$\boxed{\begin{aligned} \frac{\partial u}{\partial t} &= \frac{\partial^2 u}{\partial x^2} - uv^2 + A(1-u), \\ \frac{\partial v}{\partial t} &= 0.01\frac{\partial^2 v}{\partial x^2} + uv^2 - Bv. \end{aligned}} \tag{7.2.16}$$

In particular it describes reactions between ferrocyanide, iodate and sulphite. Typical numerical results can be found in Figure 7.12. Starting with a one pulse solution as initial condition, the solution exhibits a 'splitting' behaviour, so that after a relatively long time integration (here $t \in [0, 20000]$) we end up with more than 20 very steep pulses.

Travelling waves on the Golden-Gate Bridge

The higher-order PDE model

$$u_{tt} + u_{xxxx} + u^+ - 1 = 0 \ \text{ with } u^+ = \left\{ \begin{array}{l} u,\ u > 0, \\ 0,\ u < 0 \end{array} \right.$$
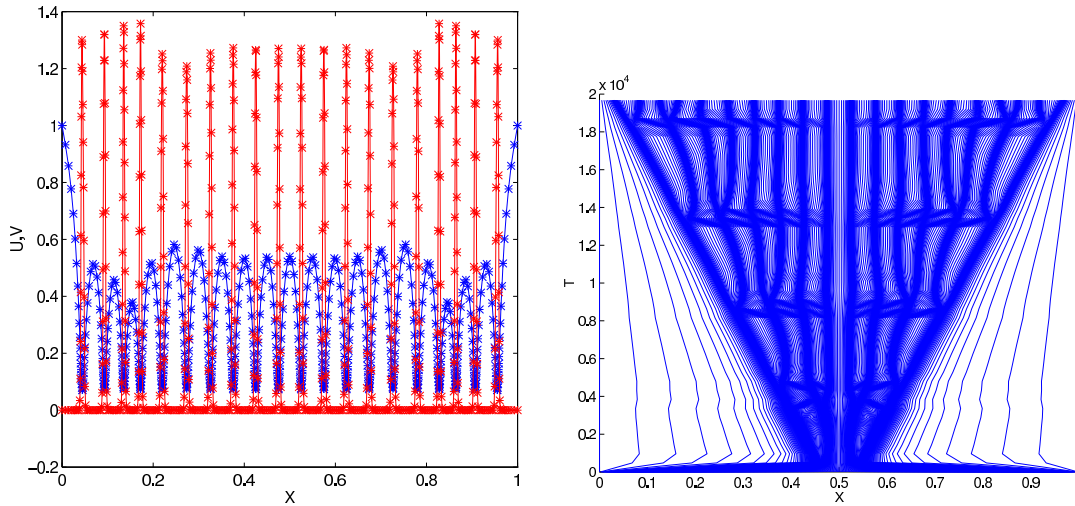
Figure 7.12: Adaptive moving grid results of model (7.2.16) with 601 grid points; solution and grid history.

has been recognized as a good model for the description of travelling wave behaviour in the Golden Gate Bridge in San Francisco. Here, the solution $u(x,t)$ represents the displacement of a beam from the unloaded state [11]. It can be re-written as a system of three first-order PDEs in the following way:

$$\boxed{\tilde{u}_t = \mathcal{A}\tilde{u}_{xx} + \mathcal{B}\tilde{u} + \mathcal{F}},$$
(7.2.17)

where $\tilde{u} := (u, v, w)^T$, $v = u_t$, $w = u_{xx}$, $\mathcal{F} = (0, u^+ - 1, 0)^T$ and

$$\mathcal{A} = \begin{pmatrix} 0 & 0 & 0 \\ 0 & 0 & -1 \\ 0 & 1 & 0 \end{pmatrix}, \quad \mathcal{B} = \begin{pmatrix} 0 & 1 & 0 \\ 0 & 0 & 0 \\ 0 & 0 & 0 \end{pmatrix}.$$

Numerical results are shown in Figure 7.13. We see interesting solution behaviour when playing with different initial data that were derived from an theoretical observation in combination with a numerical method for the stationary case. Both stable and unstable waves, but even crossing waves (in different directions) are part of the PDE model.

A tumour angiogenesis model

An application from medical sciences in which steep gradients of the solution play an important role is given by a tumour angiogenesis model for blood vessel development [12]. The PDEs read

$$\boxed{\begin{aligned} b_t + \left(\left[\frac{3}{4}c_x \right] b \right)_x &= 10^{-3}b_{xx} - 4b + 10^2 b(1-b)\max(0, c - 0.2), \\ c_t &= \delta c_{xx} - c - 10\frac{bc}{1+c}, \quad x \in [0,1]. \end{aligned}}$$
(7.2.18)

(a) Solution and (b) the moving mesh method for the 4(2,2,2) wave using the same initial data as in Figure 4. The data presented is for a run with 1501 grid points, a more accurate run with 2001 produced qualitatively the same a non-trivial task.

(a) Solution to (1) with the piecewise-linear term (2) using the fixed grid method showing the interaction of two primary waves with initial wave speeds $c = 1.1$ and -1.1. (b) The equivalent run for the exponential nonlinearity (4). (c) The same run as (b) using the moving grid method with 2001 grid points; and (d) motion of the grid (from a qualitatively identical run with 1001 grid points)

Figure 7.13: Results for a few different scenario's in the Golden-Gate model (7.2.17).

Here, b and c stand for the density of endothelial cells (blood) and the so-called tumour angiogenesis factor (TAF), respectively. For the initial and boundary conditions we have chosen:

$$c(x,0) = \cos\left(\frac{1}{2}\pi x\right), \; b(x,0) = \begin{cases} 0, & \text{if } 0 \leq x < 1 \\ 1, & \text{if } x = 1 \end{cases}$$

$$b(0,t) = 0, \; b(1,t) = 1, \; c(0,t) = 1, \; c(1,t) = 0.$$

Figure 7.14 depicts adaptive moving grid results for two values of the diffusion parameter δ: $\delta = 1$ (left panel) and $\delta = 10^{-3}$ (right panel). Decreasing the value of the diffusion coefficient makes the moving front steeper. Adaptive moving grids are therefore especially suited for this type of models from medical sciences.
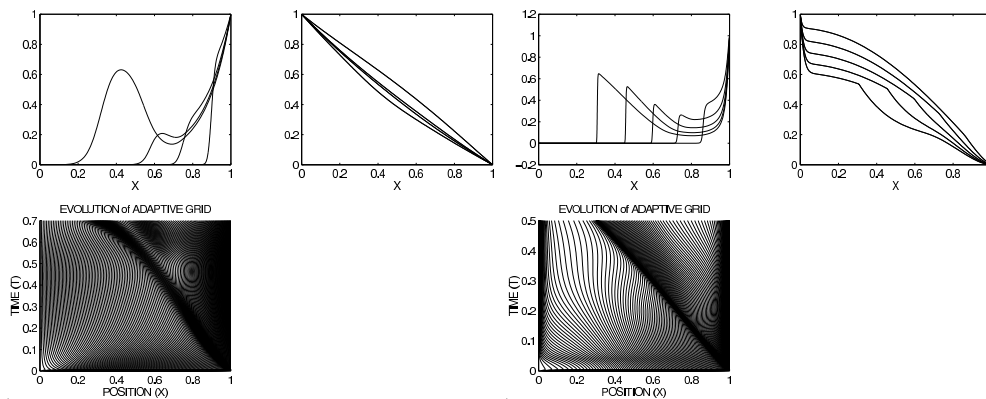
Figure 7.14: Results for two different values of the diffusion coefficient δ in model (7.2.18).

Brine transport in a porous medium

In reference [36] an application to a brine transport model in a porous medium is described (please check the details there). The model consists of two PDEs:

$$
\boxed{
\begin{aligned}
(n\rho)_t + (\rho q)_x &= 0, \quad q = -\frac{k}{\mu}(p_x + \rho g), \\
(n\rho\omega)_t + (\rho\omega q + \rho J)_x &= 0, \quad J = -\lambda|q|\omega_x,
\end{aligned}
}
\tag{7.2.19}
$$

where ω is the salt concentration in the porous medium and the fluid density ρ satisfies also the equation of state

$$
\rho = \rho_0 e^{\beta(p-p_0)+\gamma\omega}.
$$

The initial and boundary conditions for the numerical experiments in Figure 7.15 read:

$$
\omega(x,0) = 0, \ \omega(0,t) = \omega_0 > 0, \ \omega_x(1,t) = 0, \ x \in [0,L],
$$

$$
p(x,0) = p_0 \left[\left(1 - \frac{x}{L}\right) p_{left} + \frac{x}{L} p_{right} \right],
$$

$$
p(0,t) = p_0 p_{left}, \ p(1,t) = p_0 p_{right}.
$$

Different choices of p_{left} and p_{right} may result in quite different phenomena as can be seen in Figure 7.15.
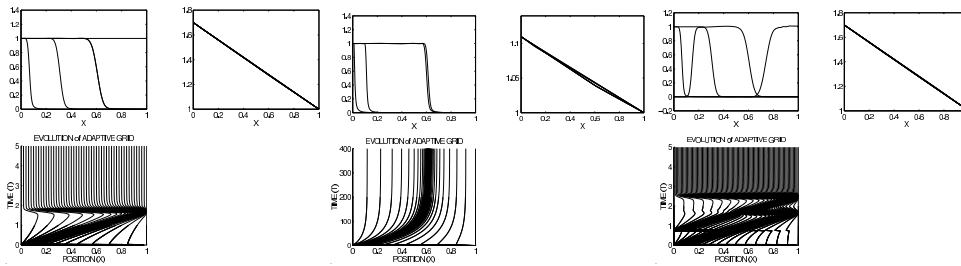
Figure 7.15: Three different cases for the brine transport model (7.2.19).

Heat flow of harmonic maps from surfaces

From theoretical mathematics a higher-dimensional PDE can be derived that deals with harmonic heat flow between the 2-disc D and the 2-sphere S:

$$
u_t = \Delta u + |\nabla u|^2 u, \ u(\mathbf{x},0) = \phi(\mathbf{x}), \ u|_{\partial D} = \phi|_{\partial D}.
\tag{7.2.20}
$$

When requiring spherical symmetry in the model $\phi(\mathbf{x}) = [\frac{x}{|\mathbf{x}|}\sin(\psi(|\mathbf{x}|)), \cos(\psi(|\mathbf{x}|))]$, it can be shown that the solution must satisfy

$$
u(\mathbf{x},t) = [\frac{x}{|\mathbf{x}|}\sin(h(|\mathbf{x}|)), \cos(h(|\mathbf{x}|))].
$$

When we substitute this expression into PDE model (7.2.20) we arrive at the much simpler PDE in one space dimension (using spherical coordinates for the 2-sphere S):

$$h_t = h_{rr} + \frac{1}{r}h_r - n^2\frac{\sin(2h)}{2r^2}$$

$$h(r,0) = \psi(r), \quad h(0,t) = 0, \quad h(1,t) = \psi(1).$$

More details on the theoretical background of the model can be read in reference [5]. Typical 'jump'-behaviour of the solution and high spatial activity around $r = 0$ is clearly seen in Figure 7.16.
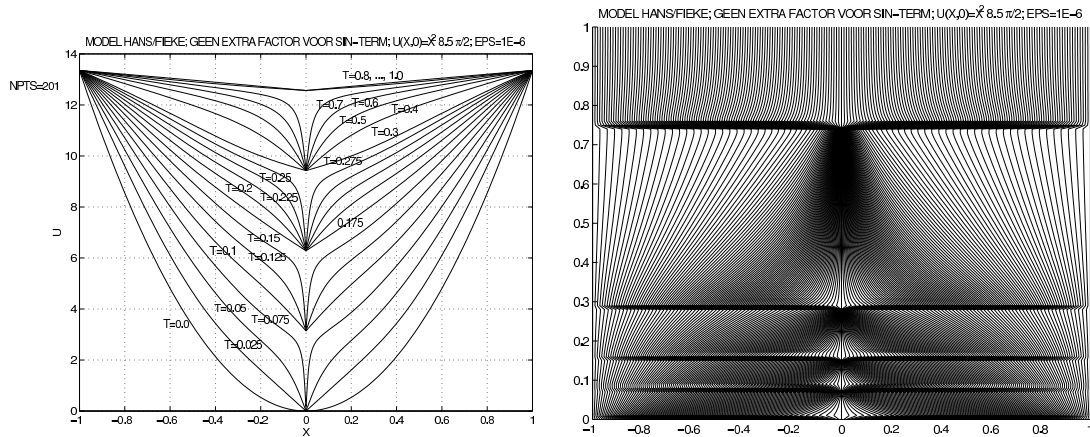
Figure 7.16: Adaptive moving grid solutions for the heat flow model (7.2.20).

The extended Fisher-Kolmogorov equation

In reference [27] a fourth-order nonlinear PDE is analyzed which may describe the propagation of domain walls in liquid crystals:

$$u_t + 10^{-8}u_{xxxx} = 10^{-4}\gamma u_{xx} + u - u^3, \quad x \in [0,1]. \tag{7.2.21}$$

The parameter γ plays an essential role, because it can be theoretically derived that for $\gamma = -3 < \gamma_* = -\sqrt{8}$ we expect multi-bump solutions. Using the conditions

$$u(x,0) = \cos(p\pi x),$$

$$u(0,t) = 1, \ u(1,t) = -1, \ u_x(0,t) = u_x(1,t) = 0.$$

interesting 'batman-ear'-type solutions can be obtained as we see in Figure 7.17. Since the fourth derivative is not included in the general 1D-code in [6], a non-uniform grid approximation of u_{xxxx} has to be worked out and fed to the time-integrator DASSL [28].
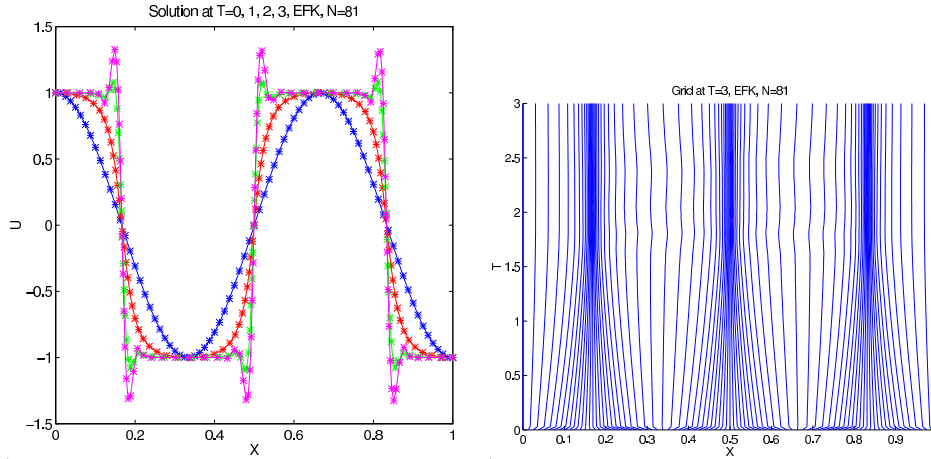
Figure 7.17: 'Batman-ear' type solutions of model (7.2.21) with 81 adaptive moving grid points.

A fifth-order Korteweg-deVries model

As a simple example, let us first consider the solution of the heat equation

$$u_t = \alpha u_{xx}$$

with coefficient $\alpha \in \mathbf{R}$ and

$$u(x,0) = \sin(\pi x), \ u(0,t) = u(1,t) = 0, \ x \in [0,1].$$

It reads $u(x,t) = e^{\alpha \pi^2 t} \sin(\pi x)$. It is easily checked that for $\alpha < 0$ we have *unstable* solutions, whereas for $\alpha \geq 0$ all solutions are *stable*. In general, for more complicated nonlinear PDE models (with physical parameters), it is often unknown whether the solutions remain stable. For this purpose numerical experiments can reveal some of the stability behaviour of the PDE solution. As a concrete example, we consider a fifth-order model for nonlinear water waves in the presence of surface tension (cf. [31] for more details):

$$\boxed{u_t + \frac{2}{15}u_{xxxxx} + (\mu u - b)u_{xxx} + (3u + 2\mu u_{xx})u_x = 0}. \tag{7.2.22}$$

We set $\mu = 1$ and simulate numerically the temporal behaviour of different scenario's, in which the parameter b can be varied. Note that for $a = \frac{3}{5}(2b+1)(b-2)$, $b \geq -1/2$ explicit solutions exist:

$$u(x,t) = 3\left(b + \frac{1}{2}\right) \operatorname{sech}^2\left(\sqrt{\frac{3(2b+1)}{4}}(x + at)\right).$$

in which $-a$ is the velocity of the wave. Other combinations, for which there are no explicit expressions, may appear as well. Figure 7.18 shows a few of these experiments. Additionally, it must be noted that these results have been obtained by working with a slightly modified version of the equidistribution principle (details in [31]), where the number of grid points is variable.
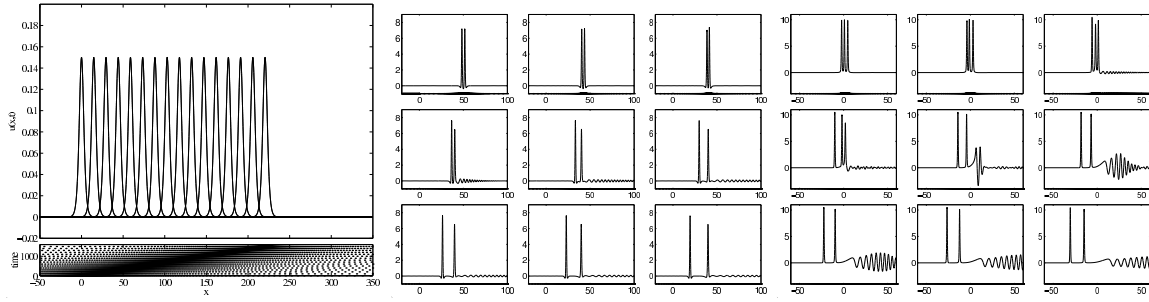
Figure 7.18: Numerical solutions of the extended KdV5 model (7.2.22) for three different scenario's.
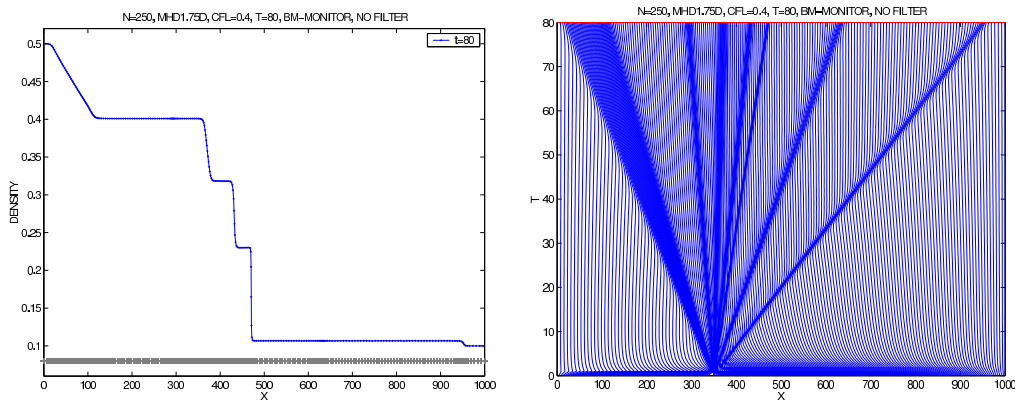
Figure 7.19: Solutions for the 1.75d mhd-shocktube model (7.2.23); left: the density at $t = 0.08$, right: grid history showing nicely the tracking of the seven different 'waves'.

An MHD shocktube model

Finally, we demonstrate the capability of the equidistribution principle when applied to a complicated system of highly nonlinear hyperbolic PDEs [15]. For this application, an alternative monitor has been used (details follow later on in a section that treats the two-dimensional case): the scaling and choice of the parameter α is done automatically. No additional smoothing as in Section smooth is needed as well. The PDE model from magneto-hydrodynamics (MHD) consists of seven PDEs:

$$\frac{\partial \rho}{\partial t} + \frac{\partial m_1}{\partial x} = 0 \quad \bar{B}_1 = \text{constant} \quad \mathbf{u} = \frac{\mathbf{m}}{\rho} \quad \mathbf{B} = (\bar{B}_1, B_2, B_3)^T$$

$$\frac{\partial m_1}{\partial t} + \frac{\partial}{\partial x} \left(\frac{m_1^2}{\rho} - \bar{B}_1^2 + (\gamma - 1)\frac{\mathbf{m}^2}{2\rho} + (2 - \gamma)\frac{\mathbf{B}^2}{2} \right) = 0$$

$$\frac{\partial m_2}{\partial t} + \frac{\partial}{\partial x}(m_1 v - \bar{B}_1 B_2) = 0 \quad \frac{\partial m_3}{\partial t} + \frac{\partial}{\partial x}(m_1 w - B_1 B_3) = 0$$

$$\frac{\partial B_2}{\partial t} + \frac{\partial}{\partial x}(B_2 u - \bar{B}_1 v) = 0 \quad \frac{\partial B_3}{\partial t} + \frac{\partial}{\partial x}(B_3 u - \bar{B}_1 w) = 0$$

$$\frac{\partial e}{\partial t} + \frac{\partial}{\partial x} \left[u \left(\gamma e - (\gamma - 1)\frac{\mathbf{m}^2}{2\rho} + (2 - \gamma)\frac{\mathbf{B}^2}{2} \right) - \bar{B}_1 \mathbf{B} \cdot \mathbf{u} \right] = 0$$

$$(7.2.23)$$

where the energy equals $e = \frac{p}{\gamma-1} + \rho\frac{\mathbf{u}^2}{2} + \frac{\mathbf{B}^2}{2}$ and

$$\gamma = \frac{5}{3}, \quad \bar{B}_1 \equiv 1, \quad \Omega = [0, 1000], \quad t \in [0, 80].$$

The initial conditions are imposed as follows (with homogeneous Neumann conditions at both ends for all components):

$$\rho|_{t=0} = \begin{cases} 0.5 & \text{for } x \in [0, 350] \\ 0.1 & \text{elsewhere} \end{cases}, \quad m_1|_{t=0} = 0$$

$$(m_2, m_3)|_{t=0} = \begin{cases} (0.5, 0.05) & \text{for } x \in [0, 350] \\ (0, 0) & \text{elsewhere} \end{cases}$$

$$B_2|_{t=0} = \begin{cases} 2.5 & \text{for } x \in [0, 350] \\ 2 & \text{elsewhere} \end{cases}, \quad B_3|_{t=0} = 0$$

$$p|_{t=0} = \begin{cases} 1 & \text{for } x \in [0, 350] \\ 0.1 & \text{elsewhere} \end{cases}.$$

The numerical results in Figure 7.19 show the density ρ at $t = 80$ and the adaptive moving grid that tracks the seven waves accurately.

7.3   The higher-dimensional case

7.3.1   A tensor-grid approach in 2D

Within this section we will adopt the alternative notation $\partial_b a$ for the partial derivative $\frac{\partial a}{\partial b}$.

Consider now the two-dimensional time-dependent PDE model

$$\partial_t u = \varepsilon \Delta u - \beta(u, x, y, t) \cdot \nabla u + s(u, x, y, t), \tag{7.3.1}$$

where $(x, y) \in [x_l, x_r] \times [y_l, y_u], \quad t \in [0, T], 0 \leq \varepsilon$ is the diffusion coefficient, β the velocity vector and s a nonlinear sourceterm.

A straightforward extension from 1D to 2D

As for the one-dimensional case, it is common and useful in structured r-refinement methods to first apply a coordinate transformation to the physical PDE model (7.3.1). Then the adaptive grid can be seen as a uniform discretization of this mapping in the new variables. For the tensor-grid case we make use of a transformation of variables ([38, 39]) in a dimensionally-split approach

$$\xi = \xi(x, t), \quad \eta = \eta(y, t), \quad \theta = t, \tag{7.3.2}$$

in which (x, y) and $(\xi, \eta) \in [0, 1] \times [0, 1]$ denote the physical and computational coordinates, respectively. Applying this transformation to equation (7.3.1) gives

$$\mathcal{J} \, \partial_\theta u - \partial_\xi u \, \partial_\eta y \, \partial_\theta x - \partial_\eta u \, \partial_\xi x \, \partial_\theta y = \varepsilon \left[\partial_\xi \left(\frac{\partial_\eta y \, \partial_\xi u}{\partial_\xi x} \right) + \partial_\eta \left(\frac{\partial_\xi x \, \partial_\eta u}{\partial_\eta y} \right) \right]$$
$$- \beta_1 \partial_\eta y \, \partial_\xi u - \beta_2 \partial_\xi x \, \partial_\eta u + s(u, x(\xi, \theta), y(\eta, \theta), \theta), \quad (7.3.3)$$

where $\mathcal{J} := \partial_\xi x \, \partial_\eta y$ is the Jacobian of the transformation (7.3.2). Note that $\partial_x \xi = [\partial_\xi x]^{-1}$ and $\partial_y \eta = [\partial_\eta y]^{-1}$ measure the grid densities in each separate direction.

The adaptive grid in terms of the mapping can be determined as a solution of two fourth-order PDEs in ξ and η with an additional time-dependent component. We set

$$\partial_\xi \left[(\mathcal{S}_1(\mathcal{J}_1) + \tau \, \partial_\theta \mathcal{J}_1) \mathcal{W}_1 \right] = 0,$$
$$\partial_\eta \left[(\mathcal{S}_2(\mathcal{J}_2) + \tau \, \partial_\theta \mathcal{J}_2) \mathcal{W}_2 \right] = 0, \quad (\tau \geq 0), \quad (7.3.4)$$

with suitable boundary conditions for x (similar conditions hold for y):

$$x(0, \eta) = x_l, \quad x(1, \eta) = x_r, \quad \partial_n x(0, \eta) = \partial_n x(1, \eta) = 0.$$

The operators $\mathcal{S}_1$ and $\mathcal{S}_2$ are direction-specific versions of the operator $\mathcal{S}$ defined as:

$$\mathcal{S} = \mathcal{I} - \sigma(\sigma + 1)(\Delta \xi)^2 \partial_{\xi\xi}^2 \quad (\sigma \geq 0), \quad (7.3.5)$$

where $\mathcal{J}_1 := \partial_\xi x$ and $\mathcal{J}_2 := \partial_\eta y$ are the 'one-dimensional' Jacobians, respectively. As mentioned before, several choices for the weight functions in (7.3.4) can be made. Here, we simply take

$$\mathcal{W}_1 = \sqrt{1 + \alpha \, \max_\eta [\partial_\xi u]^2}, \qquad \mathcal{W}_2 = \sqrt{1 + \alpha \, \max_\xi [\partial_\eta u]^2} \quad (\alpha \geq 0). \quad (7.3.6)$$

The parameter α is an adaptivity parameter: $\alpha = 0$ yields $\mathcal{W}_1 = \mathcal{W}_2 = 1$ and thus a uniform grid distribution (this can easily be derived from (7.3.4) and (7.3.5)); for increasing values of α the derivatives $\partial_\xi u$ and $\partial_\eta u$ are stressed more and more with the effect of higher spatial grid adaptation. It can be shown that the transformation (7.3.2) as a solution of equations (7.3.4), (7.3.5), (7.3.6) satisfies the 'grid-consistency' condition

$$\mathcal{J} > 0, \quad \forall \, \theta \geq 0, \text{ and } (\xi, \eta) \in [0, 1] \times [0, 1],$$

and also the 'local quasi-uniformity' property

$$\left| \frac{\partial_{\xi\xi}^2 x}{\partial_\xi x} \right| \leq 1 / \sqrt{\sigma(\sigma + 1)} \Delta \xi, \quad \left| \frac{\partial_{\eta\eta}^2 y}{\partial_\eta y} \right| \leq 1 / \sqrt{\sigma(\sigma + 1)} \Delta \eta. \quad (7.3.7)$$

The first property is equivalent to *non-singularity* of the mapping, which is, of course, a minimum demand. The second property concerns the *smoothness* of the mapping (see below for more details). Note that for $\sigma = \tau = 0$ (i.e. without smoothing operators) the grid equations (7.3.4) reduce to

$$\partial_\xi \left[\mathcal{J}_1 \mathcal{W}_1 \right] = 0, \quad \partial_\eta \left[\mathcal{J}_2 \mathcal{W}_2 \right] = 0, \quad (7.3.8)$$

which can be easily solved, just as in the one-dimensional case, to obtain an explicit expression for the (inverse) coordinate transformation

$$\xi(x,t) = \int_{x_l}^{x} \mathcal{W}_1 \, d\bar{x} / \int_{x_l}^{x_r} \mathcal{W}_1 \, d\bar{x}, \quad \eta(y,t) = \int_{y_l}^{y} \mathcal{W}_2 \, d\bar{y} / \int_{y_l}^{y_u} \mathcal{W}_2 \, d\bar{y}. \qquad (7.3.9)$$

From (7.3.8), i.e. without any kind of smoothing, follows *directly* that, as $W_{1,2} > 1$: $\mathcal{J}_{1,2} > 0$, and therefore $\mathcal{J} = \mathcal{J}_1 \mathcal{J}_2 > 0$. Using the fact that $\Delta\xi$ and $\Delta\eta$ are constant, the continuous property $\mathcal{J} > 0$ both for equations (7.3.8) and for equations (7.3.4) can be translated in semi-discrete terms as

$$\Delta x_{i,j}(\theta) > 0, \quad \Delta y_{i,j}(\theta) > 0, \quad \forall\theta \in [0,T], \quad \forall i,j. \qquad (7.3.10)$$

In other words, these relations state that the grid points can never cross one another. Property (7.3.7) can be read in semi-discrete terms as

$$\frac{1}{1 + 1/\sigma} \leq \frac{\Delta x_{i+1,j}(\theta)}{\Delta x_{i,j}(\theta)} \leq 1 + 1/\sigma, \quad \forall\theta \in [0,T], \quad \forall i,j, \qquad (7.3.11)$$

and similar relations for the y-direction. Relation (7.3.11) means that the variation in successive grid cells in both directions can be controlled by the parameter σ at every point of time.
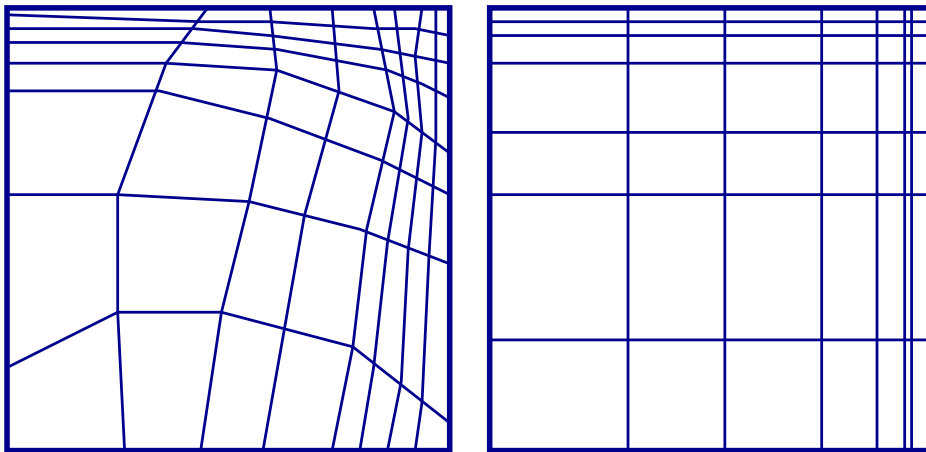
Figure 7.20: Two different types of adaptive moving grids in 2D: fully adaptive (left) vs. tensor-grid (right).

Application 1: A rotating cone

To show the effects of the adaptivity parameter α and the weight function $\mathcal{W}$ it is of interest to examine the linear parabolic equation described by

$$\partial_t u = \Delta u + f(x,y,t), \quad (x,y) \in [-1,2] \times [-1,2]. \qquad (7.3.12)$$

The source term f is chosen so that the exact solution is

$$u^*(x,y,t) = e^{-80[(x-r(t))^2 + (y-s(t))^2]},$$

Grid size	$\alpha = 0$	$\alpha = 1$, $\sigma = 0.2$	$\alpha = 1$, $\sigma = 1$	$\tilde{\alpha} = 1$, $\sigma = 0$	$\tilde{\alpha} = 10$, $\sigma = 0$
19×19	0.43590	0.71109	0.11618	0.43998	0.18423
29×29	0.25521	0.48283	0.16219	0.26116	0.03766
39×39	0.14363	0.21347	0.10206	0.15026	0.02522
49×49	0.08629	0.20423	0.08304	0.09600	0.01725
59×59	0.05636	0.09953	0.06081	0.06624	0.01147

Table 7.2: The maximum error $||e||_\infty$ at $t = 2.0$ for the rotating cone model.

where

$$r(t) = \frac{1}{4}(2 + \sin(\pi t)), \quad s(t) = \frac{1}{4}(2 + \cos(\pi t)).$$

This solution is a rotating cone with initial condition $e^{-80((x-0.5)^2+(y-0.75)^2)}$ that moves around in circles with a constant speed. During the movement, the shape of the cone does not change. Another option for the weight functions, especially for this example, could be of the form

$$\tilde{\mathcal{W}}_1 = \tilde{\mathcal{W}}_2 := \sqrt{1 + \tilde{\alpha}\, u^2}$$

to stress the solution values at the peak itself instead of the gradients. In Table 7.2 and Figure 7.21, numerical results are displayed for different choices of the weight function and the adaptivity parameters α and $\tilde{\alpha}$. A few observations can be made from these simulations. First, we see that decreasing the smoothness, i.e., taking the rather small value $\sigma = 0.2$, negatively influences the maximum error for the case of an arc-length weight function. Second, the alternative choice $\tilde{\mathcal{W}}_{1,2}$ where the solution value is emphasized, and not the gradient of the solution, gives much better numerical results, although the adaptive grids themselves, perhaps surprisingly, look not too different. Note that, if the value of $\tilde{\alpha}$ is increased, the error in the numerical solution is reduced significantly. The solutions for $\alpha = 1$ exhibit a strange decrease in amplitude both at the top of the pulse and at the foot of the pulse, although for $\sigma = 1$ this behaviour is less pronounced than for the unsmooth run with $\sigma = 0.2$. For the alternative weight function with $\tilde{\alpha} = 10$, this effect is almost annihilated. More details can be found in [38].

Application 2: A whirlpool model

$$\partial_t u = -\frac{v_t}{v_{t,max}}\frac{y}{r}\partial_x u + \frac{v_t}{v_{t,max}}\frac{x}{r}\partial_y u, \tag{7.3.13}$$

where

$$r = \sqrt{x^2 + y^2}, \;\; v_t = \frac{\tanh(r)}{\cosh^2(r)}, \;\; v_{t,max} = 0.385, \tag{7.3.14}$$

with initial and boundary conditions: $u|_{t=0} = -\tanh(\frac{y}{2})$, $\partial_n u|_{\partial\Omega} = 0$, on the domain $(x,y) \in [-4,4] \times [-4,4]$, $t \in [0,4]$. This model describes the formation of cold and warm fronts in a two-dimensional setting. Beginning with a narrow region of high gradients (a front), a fixed (in time) rotational velocity field will act to twist the front in a manner similar to that observed on daily-weather maps (positive solution values correspond to a warm front and negative values to a cold front). A complicated structure with high spatial activity, similar to a whirlpool, develops in the center of the domain. Figure 7.22 shows the grids and numerical solutions on a 49×49 grid at $t = 0.0$, 1.6, 2.8
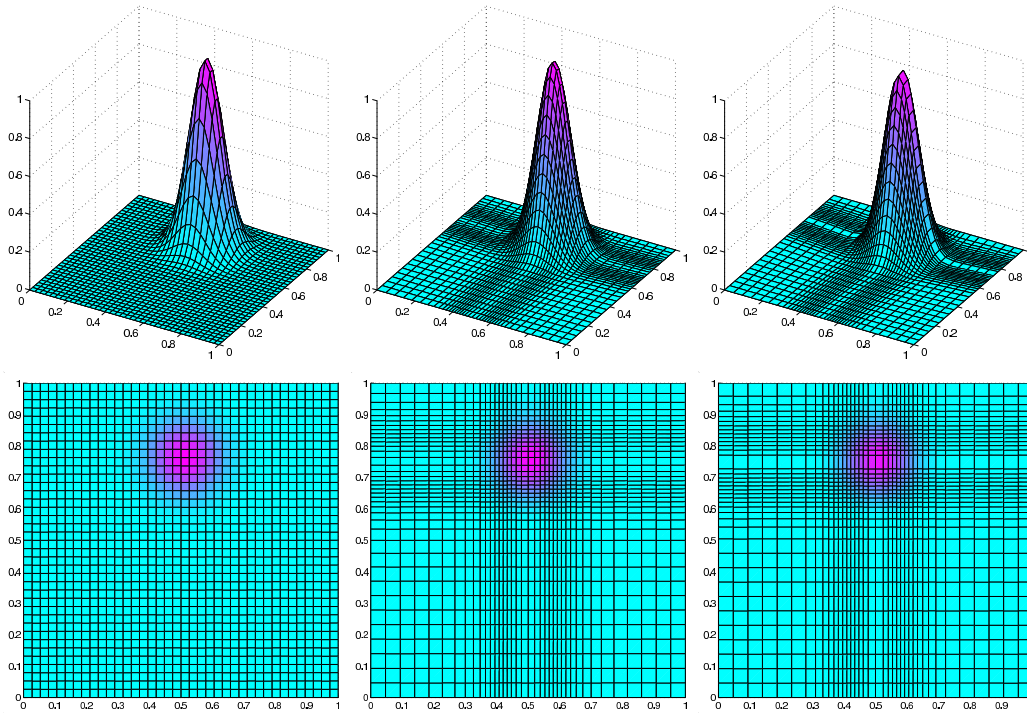
Figure 7.21: Tensor-grid solutions for the rotating cone model (7.3.12): solutions and grids after one rotation for, respectively, $(\alpha, \sigma) = (1, 0.2)$, $(\alpha, \sigma) = (1, 1)$ and $(\alpha, \sigma) = (10, 0)$.

Grid size	$\alpha = 0$	$\alpha = 1, \ \sigma = 0$	$\alpha = 1, \ \sigma = 1$	$\alpha = 10, \ \sigma = 1$
19×19	0.99983	0.57177	0.62015	0.50516
29×29	0.74773	0.27647	0.25053	0.24930
39×39	0.52421	0.15113	0.15087	0.13512
49×49	0.29419	0.10606	0.09828	0.09244
59×59	0.19357	0.08476	0.08387	0.07491

Table 7.3: The maximum error $||e||_\infty$ at $t = 4.0$ for the whirlpool model.

and 4.0. Also contourplots are given for comparison with the uniform grid and the adaptive grid case for $t = 4.0$ at which point of time the whirlpool has developed. The adaptive solution compares favorably to the uniform solution in which the inner-layer structure of the whirlpool is not resolved very well at all. Note that we haven taken here the re-scaled value $\alpha = 10$ instead of $\alpha = 1$, since the domain and the solution have larger scales. In Table 7.3 the maximum error is displayed at the final time for different values of α and σ. We see that for $\alpha = \sigma = 1$, which would be a 'standard' choice for a unit-square domain and solution values of $\mathcal{O}(1)$, the method performs not as good as for the re-scaled $\alpha = 10$ case. The difference between the smooth ($\sigma = 2$) and the non-smooth ($\sigma = 0$) case is not so profound for this model, because the steep parts of the solution remain concentrated in the centre of the domain for all time.
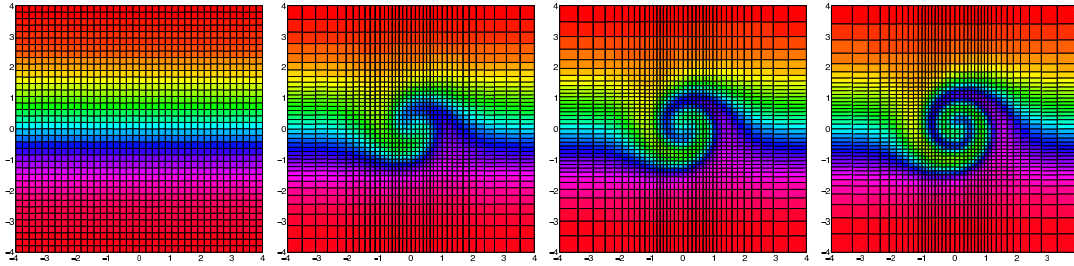
Figure 7.22: Tensor-grid solutions for the whirlpool model (7.22) at $t = 0.0, 1.6, 2.8$ and 4.0.

7.3.2 Smooth adaptive grids based on Winslow's approach

Background theory

In 2D a fully-adaptive moving grid (see Figure 7.23) can be seen as an approximation of a more general (than for the tensor-grid case) coordinate transformation between computational coordinates

$$(\xi, \eta)^T \in \Omega_c := [0, 1] \times [0, 1]$$

(with a uniform grid partitioning) and physical coordinates

$$(x, y)^T \in \Omega_p \subset \mathbb{R}^2$$

(with a non-uniform adaptive grid).
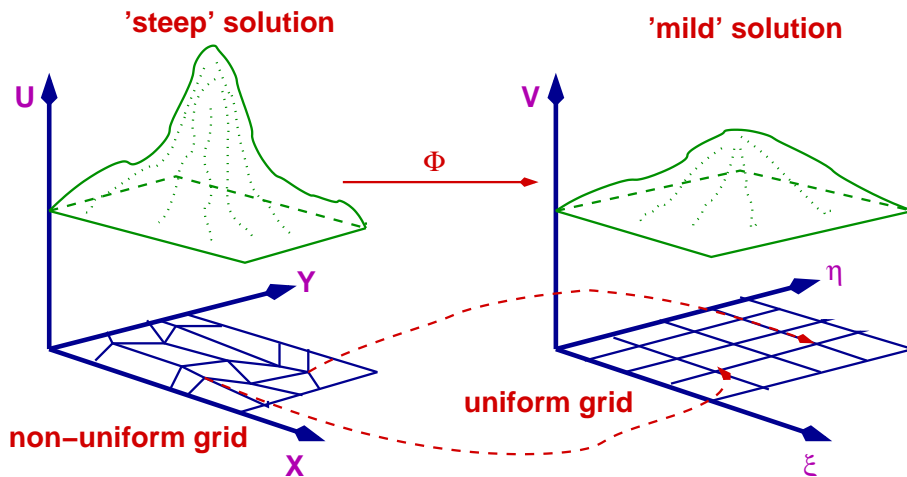
Figure 7.23: The 2D non-uniform grid seen as a 2D coordinate transformation between physical (x, y) and computational coordinates (ξ, η).

In a variational setting, a 'grid-energy' functional (à la Winslow [35]) can be defined as

$$\mathcal{E} = \frac{1}{2} \iint_{\Omega_c} \left(\nabla^T x \, \omega \, \nabla x + \nabla^T y \, \omega \, \nabla y \right) \, d\xi d\eta,$$

where $\nabla = (\frac{\partial}{\partial \xi}, \frac{\partial}{\partial \eta})^T$ and $\omega > 0$ is a monitor function.
Minimization of the energy $\mathcal{E}$ yields the Euler-Lagrange equations:

$$\boxed{\begin{aligned} \nabla \cdot (\omega \nabla x) &= 0, \\ \nabla \cdot (\omega \nabla y) &= 0. \end{aligned}} \tag{7.3.15}$$

on $\Omega_c = [0, 1] \times [0, 1]$ with boundary conditions

$$x|_{\xi=0} = x_L, \ y|_{\eta=0} = y_L, \ x|_{\xi=1} = x_R, \ y|_{\eta=1} = y_U,$$
$$\frac{\partial x}{\partial n}|_{\xi=0} = \frac{\partial x}{\partial n}|_{\xi=1} = \frac{\partial y}{\partial n}|_{\eta=0} = \frac{\partial y}{\partial n}|_{\eta=1} = 0.$$

Non-singularity of the transformation, which corresponds with non-degeneration of the grid is guaranteed by the following

Theorem 7.2. (by Clément, Hagmeijer & Sweers, '96 [13])*:*
Let $\omega \geq \tilde{c} > 0$, $\omega \in C^{0,1}(\Omega_c)$ and $\omega_\xi, \omega_\eta \in C^\gamma(\bar{\Omega}_c)$, for some $\gamma \in (0, 1)$.
$\Rightarrow \exists$ unique solution $(x, y) \in C^2(\bar{\Omega}_c)$, which is a bijection from $\bar{\Omega}_c$ into itself. Moreover, the Jacobian satisfies:
$$\mathcal{J} = x_\xi y_\eta - x_\eta y_\xi > 0.$$

Three main ingredients of their proof are the Carleman-Hartman-Winter Theorem, the Jordan Curve Theorem and the maximum principle for elliptic PDEs. In 1D system (7.3.15) reduces to the equidistribution principle from Section 7.2.2 (without additional smoothing):

$$\boxed{\underbrace{x_\xi}_{\mathcal{J}} \ \omega = \text{cst}}.$$

In that sense (7.3.15) can be seen as 2D extension to this principle. Further, the 2D system is simplified when we add an extra restriction to the transformation in the following way:

$$\boxed{\nabla(x_\xi) \cdot \nabla(y_\eta) - \nabla(x_\eta) \cdot \nabla(y_\xi) = 0 \Rightarrow \mathcal{J} \omega = \text{cst}}$$

It must also be noted that the transformation behind Winslow's method [35] is *not* a harmonic mapping, but it is *related* to it. This means that we can not use the theoretical results that are known for those classes of transformations. In fact, a counterexample can be given for the 3D (harmonic) case, for which the transformation looses its regularity (check [26] and references therein). Furthermore, several components in the proof of Theorem 7.2 can *not* be applied in 3D either. This leaves the three-dimensional case as a remaining challenge in the context of adaptive moving grids, even on simple domains such as unit cubes. However, we *will* use this concept (although the theory is not fully available) in Section 7.3.3 to show that it can be applied in practical situations.

We have seen in one space dimension that the choice of the parameter α in the monitor function ω can be a problem, since it depends on the spatial scale of the solution and the length of the domain. Furthermore, it is stationary, i.e. not time-dependent, and this could cause additional problems for models where the solution is behaving quite drastically in the time-direction. First let us define the

2D-version of the arclength monitor from Section (7.2.2):

$$\boxed{\omega = \sqrt{1 + \alpha \, \nabla u \cdot \nabla u}} \tag{7.3.16}$$

As said, α is a (problem-dependent) 'adaptivity'-parameter which controls the amount of adaptivity. Alternatively Beckett & Mackenzie [3] have defined a 'new' monitor function with a time-dependent and solution-dependent α:

$$\boxed{\omega = \alpha(t) + ||\nabla u||_2^{\frac{1}{m}}, \quad \text{with} \ \ \alpha(t) = \iint_{\Omega_c} ||\nabla u||_2^{\frac{1}{m}} \, d\xi d\eta} \tag{7.3.17}$$

Values of $m = 1$ yield better scaling and more adaptivity than for the choice $m = 2$. It is interesting to note that this idea was also briefly mentioned in [6] between the lines as a possible extension, but no implementation was given in that reference. With the 'new' monitor, application of a filter or smoother to the grid or monitor values is not necessary. Normally, smoother transitions in a general non-uniform grid can be obtained (and are needed!) by working with the smoothed value

$$
\begin{aligned}
\mathcal{S}(\omega_{i+\frac{1}{2},j+\frac{1}{2}}) \ &= \ \frac{1}{4}\omega_{i+\frac{1}{2},j+\frac{1}{2}} + \frac{1}{8}(\omega_{i+\frac{3}{2},j+\frac{1}{2}} + \omega_{i-\frac{1}{2},j+\frac{1}{2}} + \omega_{i+\frac{1}{2},j+\frac{3}{2}} + \omega_{i+\frac{1}{2},j-\frac{1}{2}}) \\
&\quad + \frac{1}{16}(\omega_{i-\frac{1}{2},j-\frac{1}{2}} + \omega_{i-\frac{1}{2},j+\frac{3}{2}} + \omega_{i+\frac{3}{2},j-\frac{1}{2}} + \omega_{i+\frac{3}{2},j+\frac{3}{2}})
\end{aligned}
$$

In the numerical experiments we denote this with *filter on* or *filter off* (working merely with $\omega_{i+\frac{1}{2},j+\frac{1}{2}}$ values i.e. $\mathcal{S}(\omega) = \omega$).

Application 3: resistive magneto-hydrodynamics

As a first application of the adaptive moving grid from the previous section, we will discuss a 2D system of MHD equations. They express the basic physical conservation laws to which a plasma must obey. Because plasma dynamics is influenced by magnetic fields through the Lorentz-force, the needed additions in going from hydrodynamic to magnetohydrodynamic behaviour is a vector equation for the magnetic field evolution and extra terms in the Euler system that quantify the magnetic force and energy density.

Using the conservative variables density ρ, momentum density $\mathbf{m} \equiv \rho\mathbf{v}$ (with velocity $\mathbf{v}$), magnetic field $\mathbf{B}$, and total energy density e, the ideal MHD equations can be written as follows (cfr. [39]):

Conservation of mass:

$$\frac{\partial \rho}{\partial t} + \nabla \cdot (\rho\mathbf{v}) = 0. \tag{7.3.18}$$

Conservation of momentum:

$$\frac{\partial(\rho\mathbf{v})}{\partial t} + \nabla \cdot (\rho\mathbf{v}\mathbf{v} - \mathbf{B}\mathbf{B}^T) + \nabla p_{tot} = 0. \tag{7.3.19}$$

Conservation of energy:

$$\frac{\partial e}{\partial t} + \nabla \cdot (e\mathbf{v} + \mathbf{v}p_{tot} - \mathbf{B}\mathbf{B}^T \cdot \mathbf{v}) = 0 \ \left[+ \varepsilon_m (\nabla \times \mathbf{B})^2\right]. \tag{7.3.20}$$

Magnetic field induction equation:

$$\frac{\partial \mathbf{B}}{\partial t} + \nabla \cdot (\mathbf{v}\mathbf{B}^T - \mathbf{B}\mathbf{v}^T) = 0 \ \left[+ \varepsilon_m \Delta \mathbf{B}\right]. \tag{7.3.21}$$

In (7.3.19) and (7.3.20) the total pressure p_{tot} consists of both a thermal and a magnetic contribution as given by

$$p_{tot} = p + \frac{\mathbf{B}^2}{2}, \quad \text{where } p = (\gamma - 1)\left(e - \rho\frac{\mathbf{v}^2}{2} - \frac{\mathbf{B}^2}{2}\right) \tag{7.3.22}$$

is the thermal pressure (notation: $\mathbf{v}^2 = \mathbf{v}^T\mathbf{v}$ and $\mathbf{B}^2 = \mathbf{B}^T\mathbf{B}$).

The terms between brackets in equations (7.3.20) and (7.3.21) extend the ideal MHD model with the effects of Ohmic heating due to the presence of currents. With the resistivity $\varepsilon_m \neq 0$, we then solve the resistive MHD equations.

The core problem is represented by the induction equation (7.3.21), alternatively written as

$$\frac{\partial \mathbf{B}}{\partial t} = \nabla \times (\mathbf{v} \times \mathbf{B}) + \varepsilon_m \Delta \mathbf{B} \tag{7.3.23}$$

with $\varepsilon_m > 0$ the resistivity or magnetic diffusion coefficient. As may be anticipated, the parameter ε_m is related to the inverse of the *magnetic Reynolds number* (also named *Lundquist number*). In two space dimensions, we set $\mathbf{B} = (B_1, B_2, 0)$, to obtain the following system of PDEs,

$$\frac{\partial B_1}{\partial t} = \varepsilon_m \Delta B_1 + v_1 \frac{\partial B_2}{\partial y} - v_2 \frac{\partial B_1}{\partial y} + B_2 \frac{\partial v_1}{\partial y} - B_1 \frac{\partial v_2}{\partial y}, \tag{7.3.24}$$

$$\frac{\partial B_2}{\partial t} = \varepsilon_m \Delta B_2 - v_1 \frac{\partial B_2}{\partial x} + v_2 \frac{\partial B_1}{\partial x} - B_2 \frac{\partial v_1}{\partial x} + B_1 \frac{\partial v_2}{\partial x}, \tag{7.3.25}$$

together with the property $\nabla \cdot \mathbf{B} = 0$.

One way to ensure a divergence-free magnetic field at all times is to make use of a vector potential formulation where $\mathbf{B} \stackrel{\text{def}}{=} \nabla \times \mathbf{A}$. From this follows automatically that $\nabla \cdot \mathbf{B} = \nabla \cdot (\nabla \times \mathbf{A}) = 0$. In two dimensional applications, the system (7.3.24)-(7.3.25) is then equivalent to the single PDE for the scalar A_3 component

$$\frac{\partial A_3}{\partial t} = -\mathbf{v} \cdot \nabla A_3 + \varepsilon_m \Delta A_3, \tag{7.3.26}$$

with $\frac{\partial A_3}{\partial y} = B_1$, $-\frac{\partial A_3}{\partial x} = B_2$, while $\mathbf{A} = (0, 0, A_3)^T$. Note that magnetic field lines are isolines of this A_3 potential.

We point out that the partial problem posed by the system (7.3.24)-(7.3.25), or equivalently the PDE (7.3.26), can be relevant as a physical solution to the special case where we consider incompressible flow $\nabla \cdot \mathbf{v} = 0$, the momentum equation (7.3.19) under the condition that the magnetic energy $\mathbf{B}^2/2$ is much smaller than the kinetic energy $\rho\mathbf{v}^2/2$, and the induction equation itself. In those circumstances, the momentum balance decouples from the magnetic field evolution. In fact, our model

then merely consists of equation (7.3.21) re-written in the potential formulation (7.3.26). In the model problems studied, we therefore prescribe an incompressible flow field $\mathbf{v}(x, y)$ as well. Starting from a uniform magnetic field, its distortion by cellular convection patterns was simulated numerically for various values of the resistivity ε_m.

One possible situation of 2D kinematic flux expulsion [41] uses an imposed four-cell convection pattern with its incompressible velocity field given by

$$\mathbf{v} = (-\sin(2\pi x)\cos(2\pi y), \cos(2\pi x)\sin(2\pi y))^T. \tag{7.3.27}$$

We then want to solve for the scalar vector potential A_3 from (7.3.26) on the domain $(x, y) \in [0, 1] \times [0, 1]$ and for times $t \in [0, 5]$. In terms of A_3, the initial uniform vertical field is obtained through $A_3|_{t=0} = 1 - x$, while the boundary conditions are $A_3|_{x=0} = 1$, $A_3|_{x=1} = 0$, $\frac{\partial A_3}{\partial n}|_{y=0} = \frac{\partial A_3}{\partial n}|_{y=1} = 0$, which corresponds with a constant initial magnetic field.

One approach, which is efficient in 1D, would be to couple the discretized systems for the adaptive grid PDEs and the physical PDE. However, there are a number of disadvantages to this approach. First, the size of the resulting system in higher space dimensions would be large and even for moderate grid densities may be prohibitive. Second, this approach does not easily admit different convergence criteria for the grid and physical solution. Further, it is not necessary to compute the grid with the same level of accuracy as the physical solution. Finally, a user may wish to control over the discretization of the physical problem and such flexibility is severely restricted by coupling the unknowns together into one large nonlinear system of equations. We have therefore decoupled the numerical solution procedure for the physical and adaptive grid PDEs, and integrate in time in an iterative manner, solving for the grid and the physical solution alternately.

For the convection-diffusion equation (7.3.26) it is appropriate to make use of an *implicit-explicit* time-integration method. The main advantage is that solving a nonlinear system, with for instance Newton's method, can be avoided, while still having reasonable stability properties, at least for mildly stiff equations. We will use within this class of integrators the first-order method 1-SBDF. Applied to (7.3.26), the discretization then reads:

$$(I - \varepsilon_m \Delta t \, \bar{\Delta}) A_3^{(n+1)} = (I - \Delta t \, \mathbf{v}^{(n)} \cdot \bar{\nabla}) A_3^{(n)}, \tag{7.3.28}$$

where $\bar{\Delta} A_3^{(n+1)}$ and $\bar{\nabla} A_3^{(n)}$ are the semi-discretized approximations of the second-order derivative and the first-order derivative terms, respectively, in equation (7.3.26). The non-symmetric linear system $\mathcal{A}^{(n)} A_3^{(n+1)} = b^{(n)}$ behind (7.3.28) is again solved with the iterative method Bi-CGSTAB with implicit diagonal preconditioning.

The MHD testcase is equation (7.3.26) with velocity field (7.3.27). The resistivity is chosen $\epsilon_m = 5 \times 10^{-4}$. In Figure 7.24 (top) the velocity field and the evolution of the parameter α from equation (7.3.16) as a function of time are displayed. Three phases can be recognized from the right plot: for small times the initially uniform magnetic field is distorted by the four convective cells to amplify the field. The magnetic field is dragged round by the motion and the field energy consequently rises. As the field grows, its scale of variation decreases until resistive effects become important. The flux is concentrated outside the eddies and so-called reconnection of the field lines takes place (second phase). In the final phase, the central field decays and a steady-state is reached. In Figure 7.25 we see at two different points of time, the solution, the adaptive grid and the magnetic field lines, respectively.

The grid is nicely concentrated in areas of high spatial activity, viz., the boundary and internal layers. Reconnection has taken place: the magnetic fieldlines have reconnected in regions of strong currents.
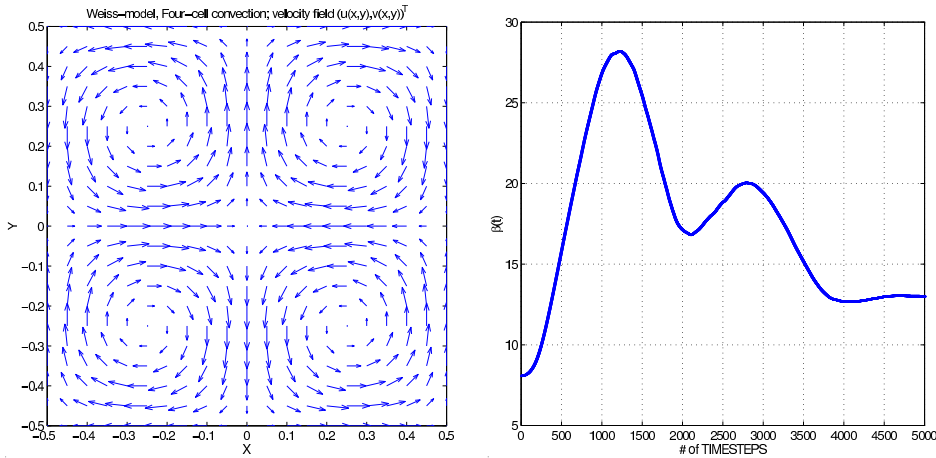
Figure 7.24: The velocity field and the (scaled) magnetic energy for model (7.3.26).

Application 4: the 2D Euler equations

The two-dimensional Euler equations of gas dynamics describing the behavior of an ideal compressible gas are written in conservative form:

$$
\frac{\partial}{\partial t}
\begin{pmatrix} \rho \\ \rho u \\ \rho v \\ E \end{pmatrix}
+ \frac{\partial}{\partial x}
\begin{pmatrix} \rho u \\ \rho u^2 + p \\ \rho u v \\ u(E + p) \end{pmatrix}
+ \frac{\partial}{\partial y}
\begin{pmatrix} \rho v \\ \rho u v \\ \rho v^2 + p \\ v(E + p) \end{pmatrix}
=
\begin{pmatrix} 0 \\ 0 \\ 0 \\ 0 \end{pmatrix},
\qquad (7.3.29)
$$

where ρ is the density, $(\rho u, \rho v)^T$ is the momentum vector, E the total energy and p the pressure. Since we are working with an ideal gas, the equation of state, which shows how the energy is related to the pressure is provided as follows: $p = (\gamma - 1)(E - \rho\frac{u^2+v^2}{2})$, with γ the ratio of specific heats. Denote $\mathbf{r} := (x, y)^T$.

Given a non-uniform partitioning $\{A_{i+\frac{1}{2},j+\frac{1}{2}}\}_{i,j}$ of the physical domain Ω_p, where $A_{i+\frac{1}{2},j+\frac{1}{2}}$ is a quadrangle with four vertices $\mathbf{r}_{i+k,j+l}$, $0 \leq k, l \leq 1$, as shown in Figure 7.26. Subdivide the computational domain $\Omega_c = \{(\xi, \eta)|\ 0 \leq \xi \leq 1,\ 0 \leq \eta \leq 1\}$ into the uniform grid:

$$(\xi_i, \eta_j)|\ \xi_i = i\Delta\xi,\ \eta_j = j\Delta\eta;\ 0 \leq i \leq I_\xi + 1,\ 0 \leq j \leq I_\eta + 1,$$

where $\Delta\xi = 1/(I_\xi + 1)$, $\Delta\eta = 1/(I_\eta + 1)$, and I_ξ and I_η are the number of grid points in the $x-$ and $y-$direction. We characterize the numerical approximations to $\mathbf{r} = \mathbf{r}(\xi, \eta)$ by $\mathbf{r}_{i,j} = \mathbf{r}(\xi_i, \eta_j)$. The elliptic system of grid PDEs is then discretized by second-order central finite differences in a straightforward manner. A Gauß-Seidel iteration method is used for the numerical solution of the resulting system of algebraic equations. The grid points on the boundary of the rectangular domain are redistributed each time step by letting them move with the same speed as the tangential component of the grid speed of the internal points adjacent to those boundary points (see [29] for more details on
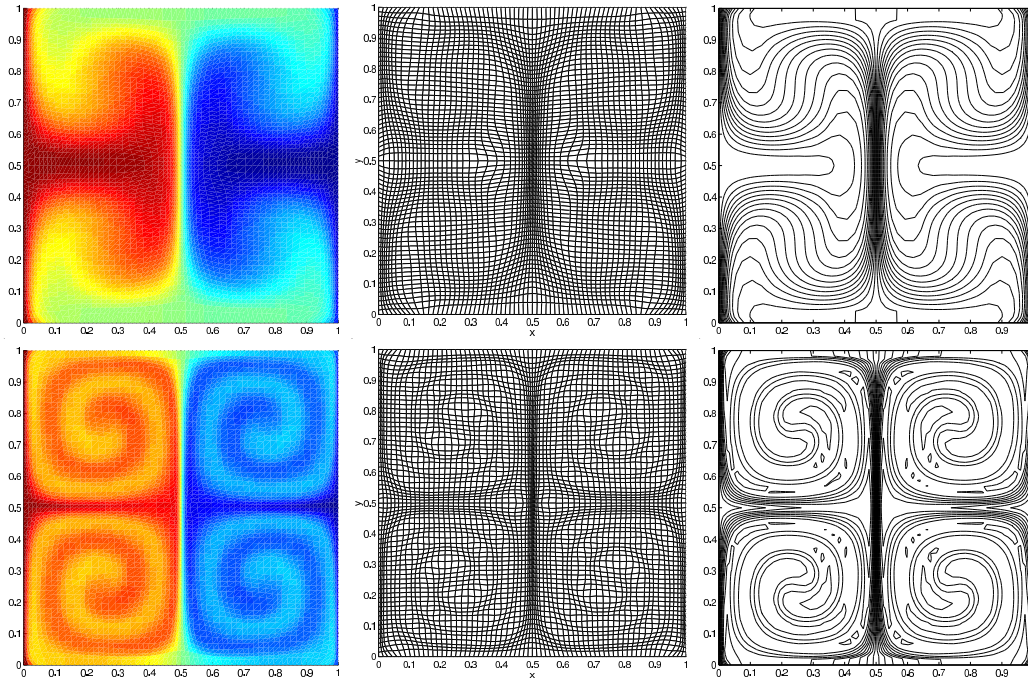
Figure 7.25: Four-cell convection results at two different points of time; left: numerical solution, middle: 2D adaptive grid, right: magnetic field lines.

this).

Having computed the new grid as described in the previous section, the solution values have to be updated on this grid by an interpolation method. In [29] a conservative interpolation method is derived to preserve conservation of mass at each grid redistribution step. Obviously, with simple linear interpolation this can not be achieved. Using a perturbation technique (see [29]) and assuming small grid speeds, it can be derived that the solution-updating scheme satisfies the following mass-conservation

$$\sum_{i,j} |\tilde{A}_{i+\frac{1}{2},j+\frac{1}{2}}| \, \tilde{\mathcal{Q}}_{i+\frac{1}{2},j+\frac{1}{2}} = \sum_{i,j} |A_{i+\frac{1}{2},j+\frac{1}{2}}| \, \mathcal{Q}_{i+\frac{1}{2},j+\frac{1}{2}},$$

where $|A|$ is the area of cell A, and $\mathcal{Q}$ and $\tilde{\mathcal{Q}}$ represent old and new numerical solution values in the physical PDE system.

Consider the two-dimensional hyperbolic conservation laws

$$\frac{\partial \mathcal{Q}}{\partial t} + \frac{\partial \mathcal{F}_1(\mathcal{Q})}{\partial x} + \frac{\partial \mathcal{F}_2(\mathcal{Q})}{\partial y} = 0, \ \ 0 < t \leq T, \tag{7.3.30}$$

subject to the initial data $\mathcal{Q}(x,y,0) = \mathcal{Q}_0(x,y)$, where T is the final time, and $\mathcal{Q}$ denotes the vector of conservative variables. $\mathcal{F}_1$ and $\mathcal{F}_2$ are the flux vectors in x- and y-direction.

Assume that a grid partitioning $\mathbf{r}_{i,j}$ of the physical domain Ω_p has been calculated. Then integrating

(7.3.30) over the finite control volume $A_{i+\frac{1}{2},j+\frac{1}{2}}$ gives (see [30] or [32])

$$\frac{\partial}{\partial t} \iint_{A_{i+\frac{1}{2},j+\frac{1}{2}}} \mathcal{Q} \, dx \, dy + \sum_{l=1}^{4} \int_{s_l} \mathbf{F}_{\mathbf{n}^l}(\mathcal{Q})|_{(x,y)\in s_l} \, ds = 0,$$

where s_l $(l = 1, ...4)$ are the four boundary segments of the cell, $\mathbf{F}_{\mathbf{n}^l}(Q) = \mathcal{F}_1 n_x^l + \mathcal{F}_2 n_y^l$ and $\mathbf{n}^l = (n_x^l, n_y^l)^T$ $(l = 1, ..., 4)$ the normal outward vectors in the finite volume (see Figure 7.26). Assuming $\mathbf{F}_{\mathbf{n}^l} = \mathbf{F}_{\mathbf{n}^l}^+ + \mathbf{F}_{\mathbf{n}^l}^-$, a general 2d finite volume scheme approximating (7.3.30) is given by

$$\mathcal{Q}_{i+\frac{1}{2},j+\frac{1}{2}}^{n+1} = \mathcal{Q}_{i+\frac{1}{2},j+\frac{1}{2}}^{n} - \frac{\Delta t}{|A_{i+\frac{1}{2},j+\frac{1}{2}}|} \Big\{ \mathcal{F}_{\mathbf{n}^1}^-(\mathcal{Q}_{i+\frac{1}{2},j-\frac{1}{2}}^n) + \mathcal{F}_{\mathbf{n}^2}^-(\mathcal{Q}_{i+3/2,j+\frac{1}{2}}^n)$$

$$+ \mathcal{F}_{\mathbf{n}^3}^-(\mathcal{Q}_{i+\frac{1}{2},j+3/2}^n) + \mathcal{F}_{\mathbf{n}^4}^-(\mathcal{Q}_{i-\frac{1}{2},j+\frac{1}{2}}^n) + \sum_{l=1}^{4} \mathcal{F}_{\mathbf{n}^l}^+(\mathcal{Q}_{i+\frac{1}{2},j+\frac{1}{2}}^n) \Big\}.$$

In the numerical experiment, we have used a local Lax-Friedrichs numerical flux, and the initial data reconstruction to improve accuracy of the scheme. More details on the numerical scheme and other applications can be found in [42].

The steps in the full solution procedure can be summarized as follows:

Step 1 Partition the computational domain Ω_c uniformly and give an initial partition of the physical domain Ω_p; compute initial grid values by a cell average of the control volume $A_{i+\frac{1}{2},j+\frac{1}{2}}$ based on the initial data $\mathcal{Q}(x, y, 0)$. In a loop over the time steps, update grid and solution and evaluate the PDE.

Step 2a Move grid $\mathbf{r}_{i,j}$ to $\tilde{\mathbf{r}}_{i,j}$ by solving the discretized grid PDEs using one Gauß-Seidel iteration.

Step 2b Compute the solution $\mathcal{Q}_{i+\frac{1}{2},j+\frac{1}{2}}$ on the new physical grid based on the conservative interpolation.
Repeat *step 2a* and *step 2b* for a fixed number of iterations.

Step 3 Evaluate the Euler equations by the finite volume method on the grid $\tilde{\mathbf{r}}_{i,j}$ to obtain the solutions $\mathcal{Q}_{i+\frac{1}{2},j+\frac{1}{2}}^{n+1}$ at time-level t^{n+1}.

Step 4 Repeat *steps 2a, 2b* and *3* until the final point of time T has been reached.

The double integral in (7.3.17) to compute the time-dependent parameter $\alpha(t)$ is approximated by applying the trapezoid rule at each time step. The test example, which is a two-dimensional Riemann problem of the Euler equations, i.e. configuration 4 in [23], has the following initial data:

$$(\rho, u, v, p)_{t=0} = \begin{cases} (1.1, 0.0, 0.0, 1.1) & \text{if } x > 0.5, \ y > 0.5, \\ (0.5065, 0.8939, 0.0, 0.35) & \text{if } x < 0.5, \ y > 0.5, \\ (1.1, 0.8939, 0.8939, 1.1) & \text{if } x < 0.5, \ y < 0.5, \\ (0.5065, 0.0, 0.8939, 0.35) & \text{if } x > 0.5, \ y < 0.5. \end{cases} \tag{7.3.31}$$

They correspond to a left forward shock, right backward shock, upper backward shock and finally a lower forward shock. The spatial domain is $[0, 1] \times [0, 1]$ and the end point of time is $t = 0.25$. Figure

7.27 shows results for the AL-monitor (7.3.16) with the 'optimized' value of the parameter $\alpha = 2$ and also for the 'full-proof' monitor (7.3.17).
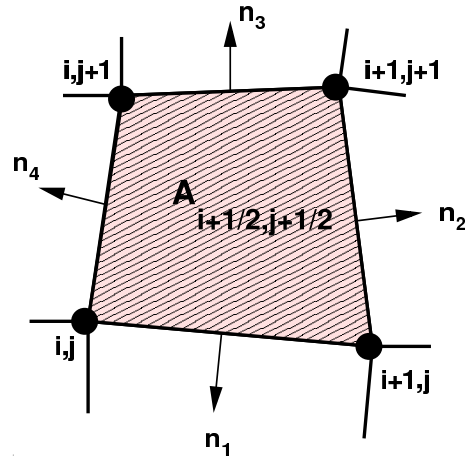
Figure 7.26: A typical non-uniform finite volume cell $A_{i+\frac{1}{2}, j+\frac{1}{2}}$.

Application 5: ideal 2D magneto-hydrodynamics

For the ideal MHD case we simply set $\eta_m = 0$ (no magnetic diffusion term) in (7.3.20) and (7.3.21). An interesting test example suitable for adaptive moving grids is the so-called Kelvin-Helmholtz instability (see [21]). This phenomenon occurs at the interface of a shear-flow configuration in 2D compressible MHD. The density at $t = 4$ and $t = 6$ using the adaptive moving grid method is displayed in Figure 7.28. Clearly, the grid is nicely concentrated near the steep parts of the rotating magnetic structures.

7.3.3 Three-dimensional adaptive moving grids

In this final section an extension of the 2D method to three space dimension is discussed.

Extension of Winslow's approach to the unit cube

Although theoretically no results are available that may guarantee the non-singularity of the mapping, we still would like to extend Winslow's method from the previous sections to 3D, and in particular to the unit cube. Straightforward calculations for the minimization of the 3D 'grid-energy' functional yields the steady-state of the PDE-system:

$$\frac{\partial x}{\partial \tau} = \nabla \cdot (\omega \nabla x)$$

$$\frac{\partial y}{\partial \tau} = \nabla \cdot (\omega \nabla y)$$

$$\frac{\partial z}{\partial \tau} = \nabla \cdot (\omega \nabla z), \quad (x, y, z)^T \in [0, 1]^3.$$
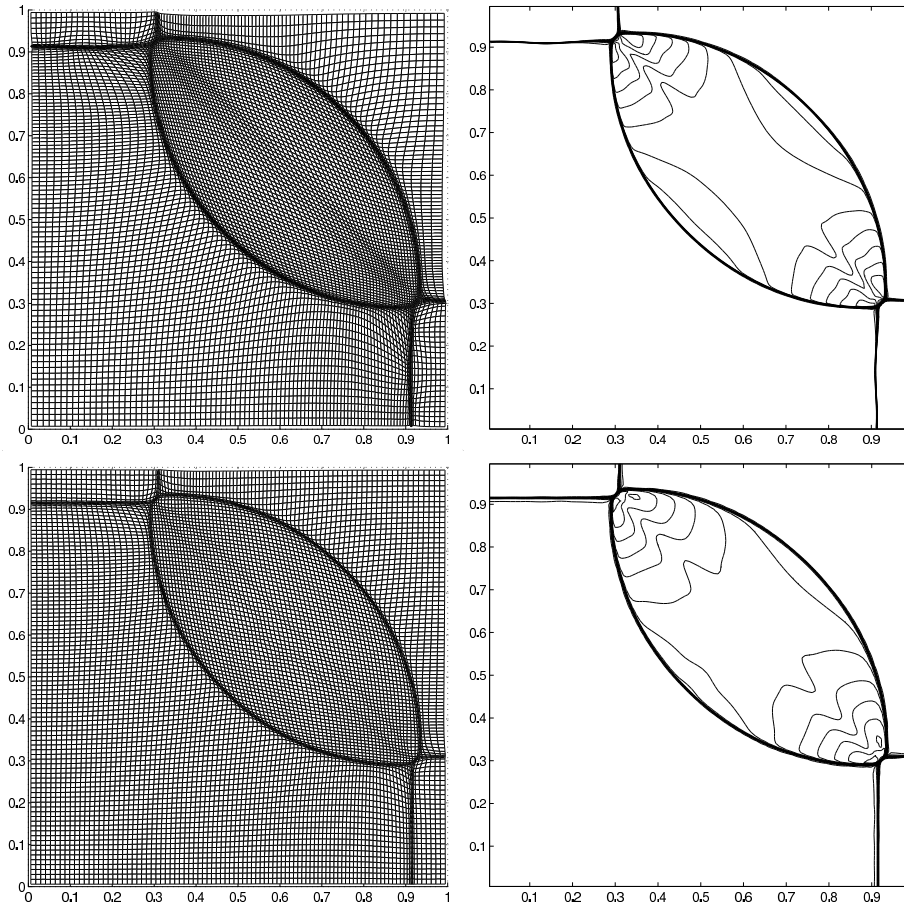
Figure 7.27: Numerical results (grid and solutions represented by contour lines) for the 2D Euler equations (7.3.29).

Here the τ denotes an artificial time variable. As in 2D, it is possible to define the monitor function with the adaptively computed constant α as follows: $\omega = \alpha(t) + ||\nabla u||_2$, $\alpha(t) = \int \int \int_{\Omega_c} ||\nabla u||_2 \, d\xi d\eta d\zeta$.

Application to a blow-up problem

The basic blow-up PDE model is in fact the reaction-diffusion PDE

$$\frac{\partial u}{\partial t} = \Delta u + u^p.$$

We first transform it via $(x, y, z, t) \rightarrow (\xi, \eta, \zeta, \theta)$; with $t = \theta$ to:

$$u_\theta + \frac{1}{\mathcal{J}} \left[u_\xi(-x_\theta(y_\eta z_\zeta - y_\zeta z_\eta) - y_\theta(x_\zeta z_\eta - x_\eta z_\zeta) - z_\theta(x_\eta y_\zeta - x_\zeta y_\eta)) + u_\eta(-x_\theta(y_\zeta z_\xi - y_\xi z_\zeta) \right.$$

$$\left. -y_\theta(x_\xi z_\zeta - x_\zeta z_\xi) - z_\theta(x_\zeta y_\xi - x_\xi y_\zeta)) + u_\zeta(-x_\theta(y_\xi z_\eta - y_\eta z_\xi) - y_\theta(x_\eta z_\xi - x_\xi z_\eta) - z_\theta(x_\xi y_\eta - x_\eta y_\xi)) \right]$$
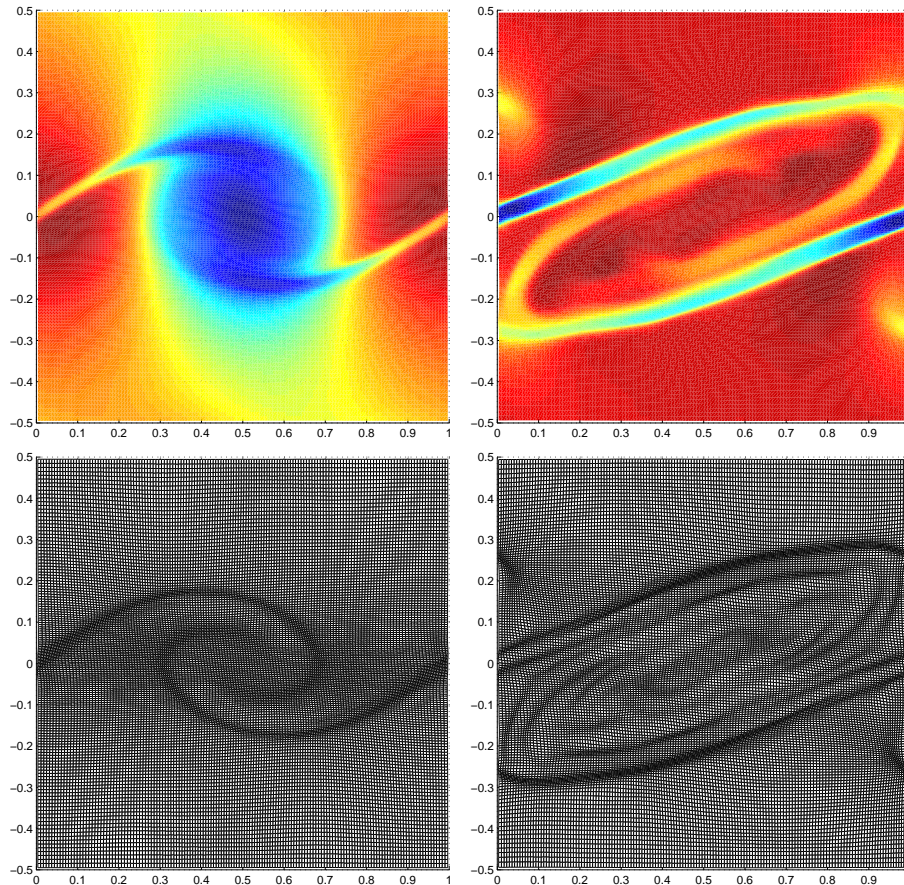
Figure 7.28: Numerical results (grid and solutions) for the 2D ideal MHD equations (7.28).

$$
\begin{aligned}
= \quad & \frac{1}{\mathcal{J}} \Bigg[\left(\frac{(y_\eta z_\zeta - y_\zeta z_\eta)^2 + (x_\zeta z_\eta - x_\eta z_\zeta)^2 + (x_\eta y_\zeta - x_\zeta y_\eta)^2}{\mathcal{J}} u_\xi \right)_\xi \\
& + \left(\frac{(y_\eta z_\zeta - y_\zeta z_\eta)(y_\zeta z_\xi - y_\xi z_\zeta) + (x_\zeta z_\eta - x_\eta z_\zeta)(x_\xi z_\zeta - x_\zeta z_\xi) + (x_\eta y_\zeta - x_\zeta y_\eta)(x_\zeta y_\xi - x_\xi y_\zeta)}{\mathcal{J}} u_\eta \right)_\xi \\
& + \left(\frac{(y_\eta z_\zeta - y_\zeta z_\eta)(y_\xi z_\eta - y_\eta z_\xi) + (x_\zeta z_\eta - x_\eta z_\zeta)(x_\eta z_\xi - x_\xi z_\eta) + (x_\eta y_\zeta - x_\zeta y_\eta)(x_\xi y_\eta - x_\eta y_\xi)}{\mathcal{J}} u_\zeta \right)_\xi \\
& + \left(\frac{(y_\zeta z_\xi - y_\xi z_\zeta)(y_\eta z_\zeta - y_\zeta z_\eta) + (x_\xi z_\zeta - x_\zeta z_\xi)(x_\zeta z_\eta - x_\eta z_\zeta) + (x_\zeta y_\xi - x_\xi y_\zeta)(x_\eta y_\zeta - x_\zeta y_\eta)}{\mathcal{J}} u_\xi \right)_\eta \\
& + ...
\end{aligned}
$$

with Jacobian $\mathcal{J} = z_\zeta(x_\xi y_\eta - x_\eta y_\xi) - z_\eta(x_\xi y_\zeta - x_\zeta y_\xi) + z_\xi(x_\eta y_\zeta - x_\zeta y_\eta)$. Note that we have not written out all terms, but merely have indicated how the structure of the different terms appears. Applications of this kind of PDE models can be found in combustion models, chemical reaction dynamics, population dynamics (motion of colonies of micro-organisms) and plasma physics (wave motion in fluids and electromagnetic fields). Let us first examine the ODE, i.e. the PDE model without diffusion

term:

$$\begin{cases} \dot{u} = u^p, \ p > 1 \\ u(0) = u_0. \end{cases} \tag{7.3.32}$$

This ODE the exact solution: $u(t) = \frac{1}{[(p-1)(T-t)]^{p-1}}$, $T = \frac{1}{u_0^{p-1}(p-1)}$ and, clearly, blows up at $t = T$ (see also Figure 7.29.
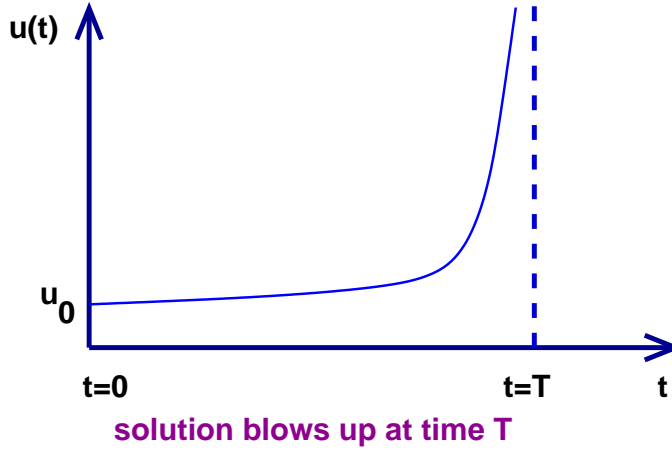
Figure 7.29: The exact solution of blow-up model (7.3.32).

It was shown by Kaplan 1963 [20] that for the PDE

$$\begin{cases} \dfrac{\partial u}{\partial t} = \Delta u + u^p, \ p > 1 \\ u|_{\partial \Omega} = 0, u(x,0) = u_0(x) \end{cases} \tag{7.3.33}$$

the following result holds: if u_0 smooth and large enough, then the solution u is regular for every $0 \leq t < T$, but

$$\lim_{t \to T} ||u(\cdot, t)||_{\mathcal{L}^\infty} = +\infty.$$

In other words, also blow up of the solution may occur, depending on the initial condition and on the value of p, despite of the fact that the Laplacian diffuses the solution. This may be illustrated by the slightly modified PDE example

$$\begin{cases} \dfrac{\partial u}{\partial t} = \dfrac{\partial^2 u}{\partial x^2} - u + u^p, \ x \in (0, \pi), \ t > 0, \\ u(x,0) = u_0(x) \geq 0, \ x \in (0, \pi), \\ u(0,t) = u(\pi, t) = 0, \ t > 0. \end{cases}$$

It can easily be shown by straightforward calculations that:
if $f = \int_0^\pi u(x,t) \sin(x) \, dx$, then $\dot{f} = \int_0^\pi (\frac{\partial^2 u}{\partial x^2} - u^p) \sin(x) \, dx - f$. Using Hölder's inequality we obtain $\dot{f} \geq -2f + \frac{f^p}{2^{p-1}}$. Now, if $f(0) > 2^{\frac{p}{p-1}}$, then $f(t) \to \infty$ in finite time and applying the inequality of Cauchy-Schwartz: $f \leq ||u||_{\mathcal{L}^2(0,\pi)} \, ||\sin(x)||_{\mathcal{L}^2(0,\pi)}$. This means that $f \to \infty$ implies $||u||_{\mathcal{L}^2(0,\pi)} \to \infty$. Thus the exact solution u leaves $\mathcal{L}^2(0, \pi)$ in finite time ('blow-up'). When we naively would apply an explicit Euler time-integration scheme with fixed time steps Δt, for example,

to the model $\left\{ \begin{array}{l} \dot{u} = u^p \\ u(0) = 1 \end{array} \right.$ we arrive at the recursion

$$u^{n+1} = u^n + \Delta t \, (u^n)^p.$$

However, the numerical solution will exist *for all* time points $t^n = n\Delta t$ (no blow-up!), whereas the exact solution exists only for finite time (see Figure 7.30). Non-uniform time steps are, therefore, crucial to capture numerically the blow-up behaviour. In this respect, Abia et al [1], has obtained theoretical results in one space dimension concerning this issue. Their result reads:
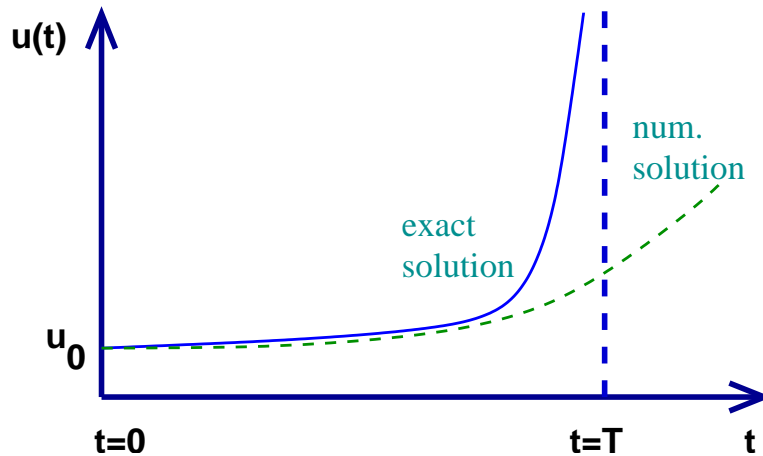
Figure 7.30: Exact vs non-adaptive numerical solution of (7.3.32).

using explicit Euler with central finite differences on a uniform spatial grid

$$\frac{u_j^{n+1} - u_j^n}{\Delta t^n} = \frac{u_{j+1}^n - 2u_j^n + u_{j-1}^n}{(\Delta x)^2} + (u_j^n)^p$$

with $\Delta t^n = \frac{\Delta\theta}{||u^n||_\infty^{p-1}}$ and constant $\Delta\theta$. Note that this can be interpreted as a Sundman *time* transformation $t(\theta) = \frac{\theta}{||u||_\infty^{p-1}}$. Then it follows that for sufficiently small Δx (with an additional time-step restriction on Δt^n due to possible numerical instabilities), the numerical solution blows up at $T_{\Delta x}$ and $\lim_{\Delta x \to 0} T_{\Delta x} = T$.

Alternatively, the solution behaviour near blow-up can also be described in terms of scaling invariance and self-similarity. In that case, consider the ODE $\dot{u} = u^2$, i.e. $p = 2$, then using a fictive computational time variable θ gives rise to a new ODE system with

$$\left\{ \begin{array}{l} \dfrac{du}{d\theta} = u, \\[2mm] \dfrac{dt}{d\theta} = \dfrac{1}{u}. \end{array} \right.$$

This ODE system is *invariant* under the scaling $t \to \lambda t$, $u \to \lambda^{-1} u$ and the numerical solution u^n uniformly approximates the true *self-similar* solution $u(t) = -\frac{1}{t}$ of the original ODE for $\Delta\theta \to 0$. This result is due to Budd, Piggott & Leimkuhler [8]. We would like to exploit these results in the

adaptive moving grid procedure, which consists of the following ingredients:

- decouple the blow-up and grid PDEs

- for the grid PDEs: use the system of heat equations with artificial time

- apply central finite differences on a non-uniform grid for the Laplacian operator Δ

- 'freeze' the non-linear terms in the PDEs at each time step

- use implicit Euler for the diffusion part in the PDE Δ and explicit Euler for the reaction term

- apply BiCGstab with ILU-preconditioning for the underlying linear systems

- use a variable Δt using the mentioned Sundman-transformation

As a testexample, we consider the initial condition

$$u(x, y, z, 0) = 10 \sin(\pi x) \sin(\pi y) \sin(\pi z),$$

with $p = 3$ in the reaction term and use, respectively, a $11^3, 21^3, \& 41^3$ spatial grid. We compare a Sundman non-uniform time step scheme with a uniform time step scheme. Figure 7.31 shows different runs and depicts the maximum value of u as a function of t. The numerical blow-up time with the adaptive moving grid with non-uniform Sundman time steps corresponds with results obtained in [25]. It is obvious that still much work has to be done in three space dimensions, especially the theoretical part deserves much attention.
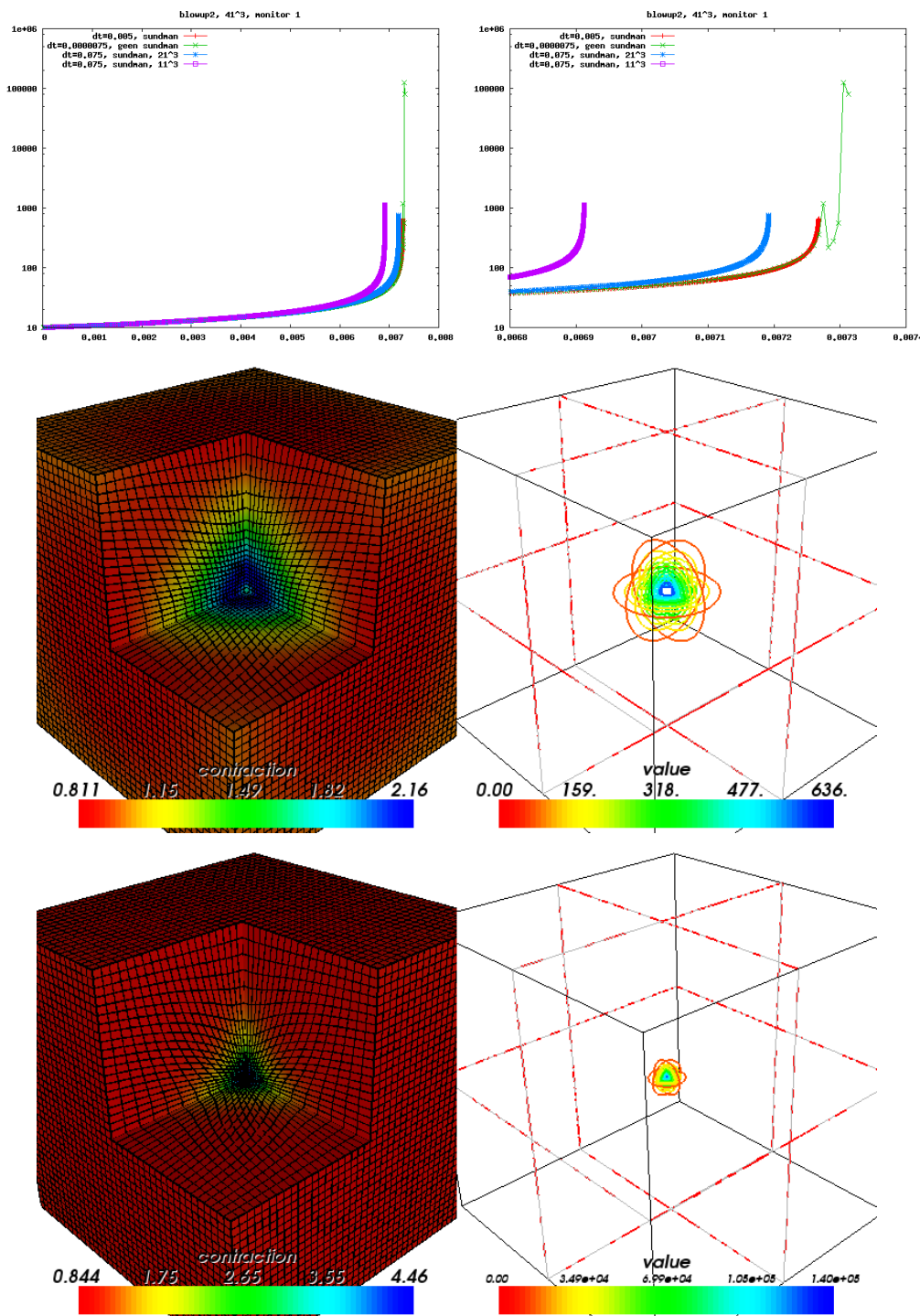
Figure 7.31: 3D adaptive moving grid results for model (7.3.33). The maximum value of u as a function of time t; blow-up time in our experiments $\sim T$ from Liang & Lin, 2005 [25]: ≈ 0.007249.

Bibliography

[1] L.M. Abia, J.C. Lópeze-Marcos & J. Martinez, The Euler method in the numerical integration of reaction-diffusion problems with blow-up, *Appl. Num. Maths.*, **38** (2001), 287-313.

[2] M. J. Baines, *Moving Finite Elements*, Clarendon Press, Oxford, 1994.

[3] G. Beckett & J. A. Mackenzie, On a uniformly accurate finite difference approximation of a singularly perturbed reaction-diffusion problem using grid equidistribution, *Comput. Appl. Math.*, **131** (2001), 381-405.

[4] M. J. Berger & J. Oliger, Adaptive mesh refinement for hyperbolic partial differential equations, *J. Comput. Phys.* **53** (1984), 484-512.

[5] J.B. van den Berg, J. Hulshof & J.R. King, Formal asymptotics of bubbling in the harmonic map heat flow, *SIAM J. of Appl. Maths.* **63** (2003), 1682-1717.

[6] J. G. Blom & P. A. Zegeling, Algorithm 731: A moving-grid interface for systems of one-dimensional time-dependent partial differential equations, *ACM Trans. in Math. Softw.*, **20** (1994), 194-214.

[7] C. de Boor, Good approximation by splines with variable knots, II, In *Springer Lecture Notes Series 363*, Springer-Verlag, New York, 1973.

[8] C.J. Budd, B. Leimkuhler & M.D. Piggott, Scaling invariance and adaptivity, *Appl. Num. Maths., Trans. on IMACS* (1999).

[9] J. U. Brackbill & J. S. Saltzman, Adaptive zoning for singular problems in two dimensions, *J. Comput. Phys.* **46** (1982), 342-368.

[10] N. Carlson & K. Miller, Design and application of a gradient-weighted moving finite element code I, in one dimension, *SIAM J. Sci. Comput.* **19** (1998), 728-765.

[11] A.R. Champneys, P.J. McKenna & P.A. Zegeling, Solitary waves in nonlinear beam equations; stability, fission and fusion, *Nonl. Dynamics*, **21** (2000), 31-53.

[12] M.A.J. Chaplain & A.M. Stuart, A model mechanism for the chemotactic response of endothelial cells to tumour angiogenesis factor, *IMA J. of Maths. Appl. in Medicine & Biology* **10** (1993), 149-168.

[13] P. Clément, R. Hagmeijer & G. Sweers, On the invertibility of mappings arising in 2D grid generation problems, *Numer. Math.* **73** (1996), 37-51.

[14] J. M. Coyle, J. E. Flaherty, R. Ludwig, On the stability of mesh equidistribution strategies for time-dependent partial differential equations, *J. Comput. Phys.* **62** (1986), 26-39.

[15] A. van Dam & P.A. Zegeling, A robust moving mesh finite volume method applied to 1d hyperbolic conservation laws from magnetohydrodynamics, *J. of Comp. Phys.*, **216** (2006), 526-546.

[16] A. Doelman, T. J. Kaper & P. A. Zegeling, Travelling waves in the 1-d self-replicating equations, *Nonlinearity* **10** (1997), 523-563.

[17] D. F. Hawken, J. J. Gottlieb & J. S. Hansen, Review of some adaptive node-movement techniques in finite-element and finite-difference solutions of partial differential equations, *J. Comput. Phys.* **95** (1991), 254-302.

[18] W. Z. Huang & W. Sun, Variational mesh adaptation II: error estimates and monitor functions, *J. Comput. Phys.* **184** (2003), 619-648.

[19] W. Z. Huang & R. D. Russell, Moving mesh strategy based on a gradient flow equation for two-dimensional problems, *SIAM J. Sci. Comput.* **3** (1999), 998-1015.

[20] S. Kaplan, On the growth of solutions of quasilinear parabolic equations, *Comm. Pure Appl. Math.* **16** (1963), 305-330.

[21] R. Keppens, G. Toth, R.H.J. Westerman & J.P. Goedbloed, Growth and saturation of the Kelvin-Helmholtz instability with parallel and antiparallel magnetic fields, *J. Plasma Phys.* **61** (1999), 1-19.

[22] P. Knupp & S. Steinberg, *Fundamentals of grid generation*, CRC-Press, Inc., 1993.

[23] P. D. Lax & X. D. Liu, Solutions of two-dimensional Riemann problems of gas dynamics by positive schemes, *SIAM J. Sci. Comput.* **19** (1998), 319-340.

[24] R. Li, T. Tang & P.-W. Zhang, Moving mesh methods in multiple dimensions based on harmonic maps, *J. Comput. Phys.* **170** (2001), 562-588.

[25] K. Liang & P. Lin, A splitting moving mesh method for 3-d quenching and blow-up problems, *Contemporary Maths.* **383** (2005), 311-324.

[26] F. Liu, S. Ji & G. Liao, An adaptive grid method and its application to steady Euler flow calculations, *SIAM J. Sci. Comput.* **20** (1998), 811-825.

[27] L.A. Peletier & W.C. Troy, *Spatial patterns; higher order models in physics and mechanics*, Birkhäuser, 2001.

[28] L. R. Petzold, A description of DASSL: a differential/algebraic system solver, In: R. S. Stepleman, eds., *IMACS Trans. on Scientific Computation*, 1983.

[29] H. Z. Tang & T. Tang, Adaptive mesh methods for one- and two-dimensional hyperbolic conservation laws, *SIAM J. Numer. Anal.* **41** (2003), 487-515.

[30] R. J. LeVeque, Finite Volume Methods for Hyperbolic Problems, Cambridge University Press, 2002.

[31] P. Saucez, A. Vande Wouwer & P.A. Zegeling, Adaptive method of lines solution for the extended fifth order Korteweg-de Vries equation, *J. of Comp. & Appl. Maths.* **183** (2005), 343-357.

[32] E. F. Toro, Riemann Solvers and Numerical Methods for Fluid Dynamics, Springer, 1999.

[33] R. A. Trompert & J. G. Verwer, A static-regridding method for two-dimensional parabolic partial differential equations, *Appl. Numer. Maths.* **8** (1991), 65-90.

[34] J. G. Verwer, J. G. Blom, R. M. Furzeland & P. A. Zegeling, A moving-grid method for one-dimensional PDEs based on the method of lines, In: J. E. Flaherty, P. J. Paslow, M. S. Shephard & J. D. Vasilakis, eds., *Adaptive Methods for Partial Differential Equations*, SIAM, Philadelphia, 1989.

[35] A. M. Winslow, Adaptive mesh zoning by the equipotential method, *Technical Report UCID* **19062** (1981).

[36] P. A. Zegeling, J. G. Verwer & J. C. H. v. Eijkeren, Application of a moving-grid method to a class of 1d brine transport problems in porous media, *Int. J. for Numer. Meth. in Fluids* **15** (1992), 175-191.

[37] P. A. Zegeling, Moving-grid methods for time-dependent partial differential equations, *CWI-tract No.94*, Centre for Mathematics and Comp. Science, Amsterdam, 1993.

[38] P. A. Zegeling, Tensor-product adaptive grids based on coordinate transformations, *J. of Comp. Appl. Maths.* **166** (2004), 343-360.

[39] P. A. Zegeling & R. Keppens, Adaptive MOL for magneto-hydrodynamic PDE models, In: Alain Vande Wouwer, Philippe Saucez, William E. Schiesser (eds.), *Adaptive Method of Lines*, Chapman & Hall/CRC Press (2001), 117-137.

[40] P. A. Zegeling & H. P. Kok, Adaptive moving mesh computations for reaction-diffusion systems, *J. of Comp. Appl. Maths.* **168** (2004), 519-528.

[41] P. A. Zegeling, On resistive MHD models with adaptive moving meshes, *J. Sci. Comput.* **24** (2005), 263-284.

[42] P.A. Zegeling, W. de Boer & H. Tang, Robust and efficient adaptive moving mesh solution of the 2-d Euler equations, *Contemporary Maths.* **383** (2005), 419-430.